RSC Advances

PAPER

View Article Online
View Journal | View Issue

Cite this: *RSC Adv.*, 2026, **16**, 24518

Humidity-dependent dielectric and electrical behavior of magnesium iron vanadate (Mg_2FeVO_6) ceramics

Mohamed I. Farouk,[a] Abdelfattah Darwish *[b] and Mohamed Morsy[c]

Received 29th March 2026
Accepted 3rd May 2026

DOI: 10.1039/d6ra02584f

rsc.li/rsc-advances

Mg_2FeVO_6 ceramic with a double perovskite-related structure was synthesized by the sol–gel method and characterized using XRD, SEM, DLS, and zeta potential. XRD identified three crystalline phases with a dominant $Ia\text{-}\bar{3}d$ structure and a crystallite size of 26.1 nm. SEM showed solid particles with an average size of ~75.6 nm. The zeta potential of −19 mV indicated negative surface charge and hydroxyl groups. A humidity sensor was fabricated by drop casting on an FTO substrate and tested across 11% to 97% RH at frequencies from 1 kHz to 5 MHz. Impedance decreased and capacitance increased with increasing RH, with the best response at 1 kHz. A capacitance sensitivity of 56.04% RH^{-1}, based on a capacitance range of 0.86 pF to 42.31 pF across 11% to 97% RH, exceeded impedance sensitivity by *a* factor of 48. The sensor showed good repeatability over four cycles and excellent short-term stability. Response and recovery times were 760 s and 25 s, respectively. Phase angle and Nyquist analysis confirmed a transition from capacitive to resistive behavior with increasing RH. Permittivity, dielectric loss, and AC conductivity increased with RH at all frequencies. The sensing mechanism involves water film formation at grain boundaries with protonic conduction *via* the Grotthuss mechanism at high RH. This work provides the first humidity-dependent dielectric and electrical dataset for Mg_2FeVO_6.

1 Introduction

Humidity sensing is critical for environmental monitoring, industrial process control, and medical devices.[1,2] Typical humidity sensors detect changes in electrical impedance or capacitance when water vapor adsorbs on a sensing layer. Common sensing materials include metal-oxide ceramics, porous silicon, and polymer films.[3,4] These materials generally cover a wide humidity range with good repeatability, but they often suffer from slow response or recovery times, cross-sensitivity to other gases, temperature dependence, and limited understanding of surface–water interactions.[3–5] Oxide perovskites have versatile dielectric and conductive properties relevant for sensing.[6] The perovskite structure (ABO_3) is a three-dimensional network of corner-sharing BO_6 octahedra. In double perovskites ($A_2BB'O_6$), two different cations occupy the octahedral B sites in an ordered rock-salt arrangement.[7–9] This B-site ordering often yields mixed-valence states or oxygen vacancies for charge balance. Such mixed-valence and defect structures can produce strong Maxwell–Wagner polarization and multiple conduction paths.[10] In Mg_2FeVO_6, the mixed valency of Fe and V cations at the B-site, combined with oxygen vacancy defects inherent to the double perovskite structure, creates the conditions for strong Maxwell–Wagner interfacial polarization. Charge carriers generated by Fe^{3+}/Fe^{2+} and V^{4+}/V^{5+} redox pairs accumulate at grain boundaries and electrode interfaces under an applied field, producing the large low-frequency permittivity and loss observed at all RH levels. This mechanism is consistent with interfacial polarization behavior reported in other mixed-valence oxide systems.[11] Adsorbed water can split into protons and hydroxide, and protons can hop through the lattice *via* the Grotthuss mechanism, which dramatically increases ionic conductivity.[12] The water adsorption at grain boundaries and active surface sites can be promoted by obtaining a well-defined homogeneous morphology with nanoscale grain size and increased surface area.[13,14]

Mg_2FeVO_6 is a double perovskite with ordered B-site cations. To our knowledge, humidity-dependent dielectric properties and sensing performance of Mg_2FeVO_6 have not been reported. A detailed study including conduction mechanisms, AC conductivity behavior, and capacitance/impedance characteristics under different relative humidity remains completely unexplored in the literature. To date, only one study has been carried out on this material (Sahu *et al.*, 2025),[9] which reported that Mg_2FeVO_6 forms a mostly cubic perovskite-like phase with

---

[a] *College of Engineering, Deanship of Scientific Research, Imam Mohammad Ibn Saud Islamic University (IMSIU), Riyadh 11432, Saudi Arabia*

[b] *Microwave Physics and Dielectrics Department, Physics Research Institute, National Research Centre (NRC), 33 El-Buhouth St., Dokki, Giza, 12622, Egypt. E-mail: abdelfatah.nrc@gmail.com*

[c] *Nanotechnology Research Centre (NTRC), The British University in Egypt (BUE), Suez Desert Road, El-Sherouk City, Cairo 11837, Egypt*

a high dielectric constant on the order of 10^4 and Maxwell–Wagner interfacial polarization.[9] The mentioned study was limited to studying the dielectric properties in a dry state only, while humidity-dependent dielectric response and sensor-level performance have never been investigated. Protonic conduction, AC conductivity, and capacitance/impedance behavior under varying RH remain unaddressed in the literature. This represents a significant research gap because the dry-state dielectric behavior already reported suggests this material has the structural and electrical features needed for humidity sensing. Therefore, this work presents the first evidence for using Mg_2FeVO_6 in humidity sensing applications.

This study synthesizes Mg_2FeVO_6 *via* sol–gel and fabricates a drop-cast sensor on an FTO substrate. Structure and morphology are characterized using XRD, SEM, DLS, and zeta potential. The viability of Mg_2FeVO_6 as a sensing material and its reaction to moisture is achieved *via* recording the changes in the material impedance and capacitance across different RH levels at multiple frequencies. Response and recovery times, repeatability, and short-term stability are reported. Phase angle and Nyquist plots are used to track the transition from capacitive to resistive behavior. AC conductivity and full dielectric spectroscopy are used to explain how water adsorption drives the sensing mechanism at each humidity stage. This provides the first systematic dataset of humidity-resolved dielectric and electrical properties for Mg_2FeVO_6, offered as a baseline for comparing this material with other double perovskite-related structures in humidity sensing.

2 Experimental

2.1 Materials

All reagents were of analytical grade and used without further purification. Ammonium metavanadate (NH_4VO_3), iron(III) nitrate nonahydrate ($Fe(NO_3)_3\cdot 9H_2O$), magnesium acetate tetrahydrate ($Mg(CH_3COO)_2)\cdot 4H_2O$, citric acid ($C_6H_8O_7$), and glacial acetic acid (CH_3COOH) were obtained from commercial suppliers. Deionized water was used in all preparations.

2.2 Sol–gel synthesis of Mg_2FeVO_6

Two solutions of $MgVO_3$ and $MgFeO_3$ were prepared separately. $MgVO_3$ solution was obtained by adding magnesium acetate tetrahydrate (7.077 g, 0.033 mol), dissolved in a water-to-acetic acid mixture at a volume ratio of 3 : 1, to ammonium metavanadate (1.930 g, 0.0165 mol), dissolved in deionized water at 80 °C, in a molar ratio of 1 : 1. The $MgFeO_3$ solution was obtained by adding iron nitrate nonahydrate (6.666 g, 0.0165 mol), dissolved in deionized water at room temperature, to ammonium metavanadate (1.930 g, 0.0165 mol), dissolved in deionized water at 80 °C, in a molar ratio of 1 : 1. Final precursor solution concentrations were 0.22 mol L^{-1} for Mg and 0.11 mol L^{-1} for each of Fe and V, targeting a nominal 5 g batch of Mg_2FeVO_6. Both $MgVO_3$ and $MgFeO_3$ solutions were kept under stirring separately for 2 hours, then combined in one vessel and stirred for a further 4 hours, during which citric acid was added at a molar ratio of 3 : 1 relative to the total moles of metal cations, giving a citric acid quantity of $3 \times (n\text{Mg} + n\text{Fe} + n\text{V}) = 3 \times 0.0495 = 0.1485$ mol. The mixture was heated to 80 °C until a viscous gel formed. The gel was dried overnight at 120 °C in air, then ground into a fine powder. The obtained Mg_2FeVO_6 powder was sintered in air at 900 °C for 6 hours and cooled naturally to room temperature. The sintering temperature of 900 °C was selected based on TGA analysis of the isostructural double perovskite Ba_2FeVO_6 (ref. 7) synthesized by the same sol–gel route, which showed that organic and carbonate intermediate decomposition was largely complete by 900 °C, indicating sufficient thermal energy for perovskite phase formation. The phase composition of Mg_2FeVO_6 at this temperature was characterized by XRD as reported in Section 3.1. The schematic representation of the synthesis procedure is presented in Fig. 1.

2.3 Measurement devices

XRD patterns were obtained using a Malvern PANalytical Empyrean 3 diffractometer (CuKα wavelength 1.5406 Å). The XRD data were collected from 10° to 80° with a step size of 0.02° and a scan rate of 2° min^{-1}. The SEM instrument (Quattro S, Thermo Scientific), operated at 20 kV, was used to obtain morphological features. The SEM images were captured at two different magnifications: 25 000× (scale bar = 2 μm) and 100 000× (scale bar = 1 μm). The Malvern Panalytical Zetasizer was used for dynamic light scattering (DLS) size distribution and zeta potential measurements. For the DLS measurement, the sample was dispersed in deionized water (0.1 gm ml^{-1}) using an ultrasonic bath for 10 min. The measurements were carried out three times at 25 °C, and then the average particle size distribution was reported. For zeta potential, the sample was measured using folded capillary cells, with five replicate measurements. The dielectric properties were measured using a HIOKI-3532-50 LCR bridge over a frequency range of 1 kHz to 5 MHz with an applied AC signal of 1 V. Below 1 kHz, the impedance of the sensing layer approached and exceeded the instrument's upper measurement limit of 200 MΩ, and no reliable data were obtained in this region. All measurements were performed at room temperature.

2.4 Sensor fabrication and testing

The humidity sensor has been fabricated using the drop casting method. The humidity sensing material was mixed with a small amount of 1% PVA solution and ground to form a paste, then deposited over a pre-cleaned fluorinated tin oxide (FTO) substrate. The sensor was allowed to dry at 150 °C for 12 hours, and then the sensor was conditioned at 11% RH and 97% RH for an additional 24 hours. The required RH level was maintained constant inside a sealed conical flask containing saturated salt solutions. The saturated salt solutions were prepared by dissolving analytical grade salts in de-ionized water. The required relative humidity was obtained following the methodology of ASTM E104-02.[15,16] Lithium chloride, potassium acetate, potassium carbonate, sodium chloride, potassium chloride, and potassium sulfate were used to generate 11% RH, 23% RH, 43% RH, 75% RH, 84% RH, and 97% RH, respectively. The fabricated sensor was suspended over a saturated salt

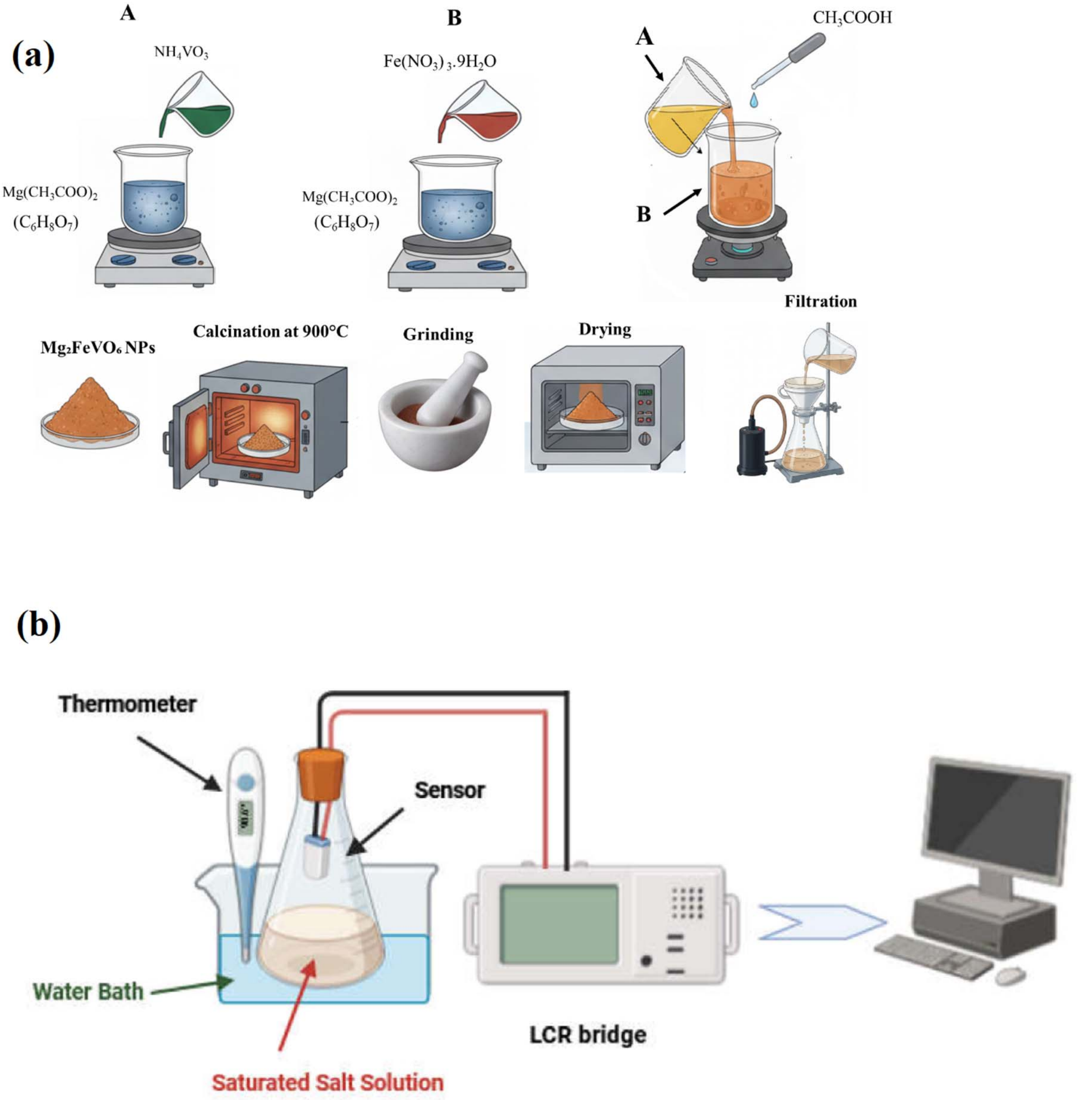

Fig. 1 Schematic diagrams of the Mg_2FeVO_6 synthesizing method (a) and the experimental setup for humidity sensor testing using a saturated salt solution and an LCR bridge (b).

solution and allowed to stabilize at each level for 30 minutes. Once the impedance value of the sensor remained constant or fluctuated within 3%, the corresponding impedance value was recorded using the HIOKI-3532-50 LCR bridge. The reported data is the average of three measurements taken each one-minute interval at each RH level. The sensor was tested by applying an AC voltage of 1 V for all impedance/capacitance measurements across all frequencies from 1 kHz up to 5 MHz. All tests have been performed at room temperature.

3 Results and discussion

3.1 XRD analysis

X-ray diffraction patterns collected over the 2θ range of 10° to 90° using Cu Kα radiation ($\lambda = 1.5419$ Å) for the prepared magnesium iron vanadate ceramics are presented in Fig. 2. The pattern shows sharp, well-defined peaks with no broad amorphous background, confirming that crystalline phases formed at 900 °C. Twenty-five diffraction peaks were identified in this range, and all 25 are accounted for with zero unassigned reflections. Three phases are present: a dominant cubic $Ia\bar{3}d$ population (Phase A, 17 peaks), a minor second $Ia\bar{3}d$ population of the same compound (Phase B, 5 peaks), and the secondary vanadate $Mg_2V_2O_7$ (3 peaks). Phase identification was carried out in two stages: geometric indexing of all 25 observed reflections against candidate space groups and standard reference data, establishing the structural model independently of any profile fitting; followed by Le Bail profile refinement to obtain refined lattice parameters, reliability factors, and quantitative phase fractions. The geometric

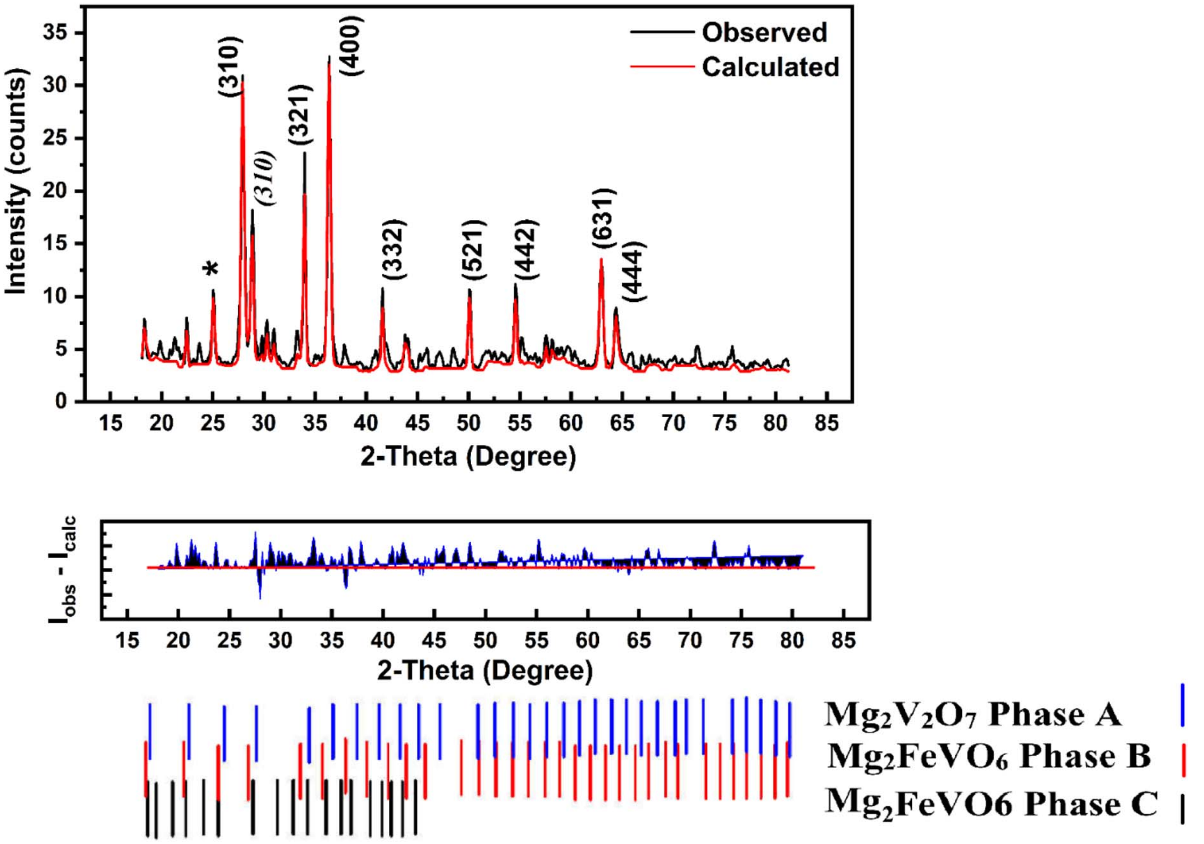

Fig. 2 Le Bail profile analysis of the magnesium iron vanadate ceramic sintered at 900 °C. Upper panel: observed pattern (black) and Le Bail calculated profile (red) on an absolute intensity scale; selected Miller indices (*hkl*) are shown for the strongest reflections of Phase A *Ia*-$\bar{3}$*d* (regular type), Phase B *Ia*-$\bar{3}$*d* (italic type), and $Mg_2V_2O_7$ (asterisk). Lower panel: residual difference curve ($I_{obs}-I_{calc}$, blue). The refinement accounts for three crystalline phases: Phase A *Ia*-$\bar{3}$*d* Mg_2FeVO_6, Phase B *Ia*-$\bar{3}$*d* Mg_2FeVO_6, and $Mg_2V_2O_7$ (ICDD 00-029-0877). Complete peak assignments for all 25 reflections are provided in Table S1 (SI). Reliability factors: $R_p = 31.77\%$, $R_{wp} = 41.12\%$, $R_{exp} = 69.08\%$, $\chi^2 = 0.354$.

indexing provides the model-independent foundation; the Le Bail refinement provides quantitative confirmation and precision. Le Bail refinement yields lattice parameters, quantitative phase fractions, and reliability factors without requiring atomic coordinates, and represents an accepted method for phase quantification when a structural model is unavailable.[17–19] The phase identification and complete peak assignments are summarized in Table S1 and Fig. S1 (SI).

The space group is established by systematic absences, independently of any profile refinement. Every candidate space group for an ordered $A_2BB'O_6$ double perovskite was evaluated against the observed pattern. The disordered simple perovskite *Pm*-$\bar{3}$*m* (No. 221) carries no extinction rule and therefore requires reflections with $h + k + l =$ odd to be present throughout the pattern; these are absent throughout, excluding this model unambiguously. The rock-salt-ordered *Fm*-$\bar{3}$*m* (No. 225) requires the (111) ordering reflection at $2\theta = 15.15°$ ($d = 5.847$ Å) to be present as the dominant low-angle superstructure peak; no peak is observed anywhere between 14.5° and 15.5°, excluding *Fm*-$\bar{3}$*m* and with it the rock-salt B-site arrangement adopted by the Ba analogue Ba_2FeVO_6. Tetragonal *I*4/*m* (No. 87) requires all reflections with $h \neq l$ to appear as resolved doublets; no splitting is observed anywhere in the pattern, all reflections indexing as single cubic lines. Monoclinic $P2_1/n$ (No. 14) requires additional low-angle reflections violating the body-centering condition; the strict body-centering condition $h + k + l = 2n$ is satisfied by all 22 Mg_2FeVO_6 peaks without exception, excluding monoclinic distortion. All four *Ia*-$\bar{3}$*d* extinction conditions are satisfied simultaneously across all 22 Mg_2FeVO_6 peaks within ±2.5%, uniquely identifying *Ia*-$\bar{3}$*d* (No. 230) as the space group. The key diagnostic is the complete absence of the *Fm*-$\bar{3}$*m* (111) peak at $2\theta = 15.15°$: this single absence eliminates rock-salt ordering and, combined with strict body-centering across all 22 reflections, uniquely confirms *Ia*-$\bar{3}$*d*.

The rejection of orthorhombic models warrants an explicit statement. *Pnma* cannot account for Peak 6 ($d = 3.182$ Å, $I = 50.73\%$), the 3rd most intense peak in the entire pattern: fitting it to any *Pnma* reflection would require a *d*-spacing error exceeding 3.5%, well outside the ±2.5% geometric indexing tolerance. *Ia*-$\bar{3}$*d* accounts for it naturally as the (310) ordering reflection of Phase B at $d_{calc} = 3.2606$ Å (error $= -2.42\%$). $P2_1/n$ is excluded by the strict body-centering condition $h + k + l = 2n$ satisfied by all 22 Mg_2FeVO_6 peaks without exception. No orthorhombic cell was found that matched all 25 observed peaks within ±2.5%.

Phase identification against standard reference data confirms the three-phase assignment. The dominant $Ia\text{-}\bar{3}d$ Mg_2FeVO_6 phase carries no published ICDD reference card; its identification rests on the systematic absence analysis detailed above, which uniquely and model-independently establishes $Ia\text{-}\bar{3}d$ symmetry—a conclusion that no profile refinement can strengthen or undermine. The secondary phase $Mg_2V_2O_7$ is identified against ICDD reference pattern 00-029-0877 (triclinic $P\text{-}\bar{1}$); three peaks at $2\theta = 17.349°$ ($d = 5.107$ Å, $\Delta = -0.36\%$), 22.728° ($d = 3.909$ Å, $\Delta = +0.33\%$), and 24.156° ($d = 3.681$ Å, $\Delta = -0.34\%$) match ICDD positions within ±0.4% and are not predicted by any $Ia\text{-}\bar{3}d$ reflection, providing unambiguous identification. At $2\theta = 24.156°$, $Mg_2V_2O_7$ ($\bar{3}11$) at $d = 3.684$ Å and Fe_2O_3 (012) at $d = 3.684$ Å are coincident within experimental resolution; $Mg_2V_2O_7$ is the preferred assignment on stoichiometric grounds, as atomic-level cation mixing in the sol–gel precursor makes unreacted single-oxide Fe_2O_3 an improbable source of secondary phase, and $Mg_2V_2O_7$ is the expected vanadium-rich crystallization product when V^{5+} is not fully incorporated into the double perovskite-related structure during the 900 °C anneal. Regarding hematite Fe_2O_3 (ICDD 00-033-0664, $R\text{-}\bar{3}c$): all Fe_2O_3 reference lines overlap with $Ia\text{-}\bar{3}d$ Mg_2FeVO_6 reflections within ±2.5%, leaving no diagnostic peak; Fe_2O_3 is neither confirmed nor excluded, and minor traces cannot be ruled out on the basis of d-spacing analysis alone. It is important to acknowledge that the two-population $Ia\text{-}\bar{3}d$ model, while physically motivated and consistent with all 25 observed reflections within the stated tolerances, relies in part on a small number of weak reflections assigned to Phase B and cannot be considered unique on the basis of powder diffraction data alone.

With the space group established, lattice parameters were determined by least-squares refinement of d-spacings from indexed reflections using the cubic relation $d = a/\sqrt{N}$ (where $N = h^2 + k^2 + l^2$), with uncertainties reported as one standard deviation. Phase A yields $a = 10.128 \pm 0.121$ Å from 17 indexed peaks; Phase B yields $a = 10.311 \pm 0.159$ Å from 5 peaks. The two populations differ by $\Delta a = 0.304$ Å ($\Delta a/a = 3.01\%$) from refined parameters, compared with $\Delta a = 0.183$ Å ($\Delta a/a = 1.81\%$) from geometric indexing; the larger refined separation reflects the precision gain of full-profile fitting and falls within the combined geometric uncertainty of ±0.200 Å derived from the quadrature sum of the individual geometric standard deviations. The subcell relation gives $a_{\text{sub}} = a/2 = 5.049$ Å for Phase A and 5.201 Å for Phase B, both consistent with $A_2BB'O_6$ double perovskite-related stoichiometry. Both populations display identical $Ia\text{-}\bar{3}d$ symmetry and both carry ordering reflections, confirming that Phase B is not a disordered impurity or a distinct crystalline phase but a second ordered $Ia\text{-}\bar{3}d$ population of the same compound. The subcell relation gives $a_{\text{sub}} = a/2 = 5.064 \pm 0.061$ Å, consistent with $A_2BB'O_6$ double perovskite-related stoichiometry. The indexing was performed geometrically using observed d-spacings matched to calculated positions from the cubic $Ia\text{-}\bar{3}d$ cell; of the 22 indexed Mg_2FeVO_6 peaks, 19 match within ±2.0% and 3 (Peaks 5, 6, and 12) sit at ±2.0–2.5%, at the tolerance boundary. These three boundary peaks include the two strongest ordering reflections, whose positions motivated the two-population model rather than forcing a poorer single-cell fit. Peak 5 ($2\theta = 27.070°$, $I = 94.70\%$) sits marginally outside the stated ±2.5% tolerance at +2.77%; its assignment as the (310) ordering reflection of Phase A is nonetheless unambiguous, no alternative phase in the pattern accounts for a peak of this intensity at this position, and it is forbidden in both $Pm\text{-}\bar{3}m$ and $Fm\text{-}\bar{3}m$. Peak 12 ($2\theta = 40.905°$, $I = 25.46\%$) indexed as (332) with +2.10% error falls within the acceptable ±2.5% range; the minor deviation is consistent with partial overlap with the $Mg_2V_2O_7$ secondary phase or instrumental broadening at higher angles. Complete peak indexing for all 25 observed peaks is provided in Table S1.

The geometric values of lattice parameters were determined by least-squares refinement for Phase A: $a = 10.128 \pm 0.121$ Å from 17 indexed peaks and for Phase B: $a = 10.311 \pm 0.159$ Å from 5 peaks. These values served as starting parameters for Le Bail profile refinement performed against the full powder pattern over the 2θ range 17–90° using Cu Kα_1 radiation ($\lambda = 1.5406$ Å), with peak profiles described by a pseudo-Voigt function with Caglioti half-width parameterization ($\text{FWHM}^2 = U\tan^2\theta + V\tan\theta + W$; refined: $U = 0.4261$, $V = -0.2257$, $W = 0.1204$, $\eta = 0.111$). The refinement converged to Phase A: $a = 10.098 \pm 0.025$ Å and Phase B: $a = 10.402 \pm 0.004$ Å; the shifts from geometric starting values fall within the uncertainty bounds of the geometric method (±0.121 Å and ±0.159 Å respectively) and reflect the superior precision of full-profile fitting over single-peak d-spacing analysis. The reliability factors of the Le Bail fit are $R_p = 31.77\%$, $R_{wp} = 41.12\%$, $R_{exp} = 69.08\%$, and $\chi^2 = 0.354$. It is noted that Le Bail profile fitting is a pattern-decomposition method that refines lattice parameters and profile shape without atomic coordinates or structural constraints; R-factors from Le Bail fitting are therefore not directly comparable to those from full Rietveld refinement and are systematically higher for equivalent data quality. The elevated R_{wp} reflects the multi-phase peak overlap region at 28–33° and the limited counting statistics of the dataset rather than a deficiency in the structural model; the $\chi^2 < 1$ indicates that measurement uncertainties are conservatively estimated, consistent with low-count data collection, and both figures are reported here for transparency. Full Rietveld refinement, including B-site order parameter quantification and M–O bond length determination, requires a reliable atomic coordinate starting model. The only published $Ia\text{-}\bar{3}d$ phase reported for Mg_2FeVO_6 by Sahu *et al.* carries $a = 12.43$ Å, substantially exceeding the double perovskite range and falling within the garnet lattice parameter range ($a \approx 12$–13 Å); its atomic coordinates are therefore not transferable as a starting structural model for the present $a \approx 10.1$ Å phase, and construction of a reliable starting model requires either *ab initio* structure solution or a dedicated future study. Full Rietveld refinement is accordingly identified as a priority for future work. All subsequent structural discussion uses the refined lattice parameters.

The most significant crystallographic finding is evidence consistent with Fe/V B-site ordering in the $Ia\text{-}\bar{3}d$ structured Mg_2FeVO_6. In an $A_2BB'O_6$ double perovskite, ordering of two

Table 1 Superstructure ordering reflections ($I \geq 5\%$), forbidden in disordered simple perovskite ($Pm\text{-}\bar{3}m$) and permitted in $Ia\text{-}\bar{3}d$. ★ = Among the strongest peaks in the pattern; † = error at ±2.0–2.5% tolerance boundary. d_{calc} calculated from cubic $Ia\text{-}\bar{3}d$, a = 10.128 Å (Phase A) or 10.311 Å (Phase B). Peaks 5 and 6 form the decisive (310) doublet pair proving B-site cation ordering in both populations

Peak	$2\theta_{\text{obs}}$ (°)	d_{obs} (Å)	I (%)	hkl	d_{calc} (Å)	Δ (%)	Phase	Type	Note
5	27.070	3.2913	94.70	(310)	3.2026	+2.77	A	O	★
10	33.190	2.6971	67.60	(321)	2.7067	−0.36	A	O	★
6	28.023	3.1815	50.73	(310)	3.2606	−2.42	B	O	★ †
20	62.544	1.4839	31.50	(631)	1.4932	−0.62	A	O	
12	40.905	2.2045	25.46	(332)	2.1592	+2.10	A	O	†
17	49.483	1.8405	24.21	(521)	1.8490	−0.46	A	O	
2	21.525	4.1249	16.07	(211)	4.1346	−0.23	A	O	
9	32.447	2.7571	11.64	(321)	2.7557	+0.05	B	O	
23	71.982	1.3108	6.60	(730)	1.3298	−1.43	A	O	
16	47.882	1.8983	5.91	(521)	1.8825	+0.84	B	O	

chemically distinct cations on the B-site creates a supercell doubled relative to the simple perovskite subcell. This doubling generates superstructure reflections at positions that are symmetry-forbidden in both the disordered $Pm\text{-}\bar{3}m$ structure and the rock-salt-ordered $Fm\text{-}\bar{3}m$ structure; their observation therefore constitutes model-independent evidence that Fe and V occupy alternating octahedral sites. The present pattern contains 14 confirmed ordering reflections—10 in Phase A and 4 in Phase B—of which the 10 most significant ($I \geq 5\%$) are listed in Table 1. Geometric indexing (Table 1) establishes space group $Ia\text{-}\bar{3}d$ independently of profile refinement, providing model-free validation of the Le Bail structural model.

The intensity distribution is unambiguous: the (310) reflection of Phase A at $2\theta = 27.070°$ is the 2nd most intense peak in the entire pattern ($I = 94.70\%$), forbidden in both $Pm\text{-}\bar{3}m$ and $Fm\text{-}\bar{3}m$, and the (321) reflection at $2\theta = 33.190°$ is the 3rd most intense ($I = 67.60\%$). The quantitative ordering indicator for Phase A, the ratio of total ordering-reflection intensity to total fundamental-reflection intensity, is $\Sigma I(\text{ord})/\Sigma I(\text{fund}) = 278.1/175.2 = 1.59$. This ratio is proportional to $S^2\,(f_{\text{Fe}} - f_{\text{V}})^2$, where S is the B-site order parameter (0 = fully disordered, 1 = perfectly ordered) and f denotes the X-ray atomic scattering factor. A value of 1.59, exceeding unity, indicates that long-range Fe/V ordering is present; Rietveld refinement is required to quantify the order parameter S numerically. It is noted that the ordering reflection count of 14 confirmed reflections (10 Phase A, 4 Phase B) derives from the complete geometric analysis over 10–90°; the Le Bail profile fitting over 17–90° resolves 12 of these reflections directly, with the two Phase B ordering reflections (431) at $2\theta = 44.859°$ and (521) at $2\theta = 47.882°$ falling below the reliable profile-fitting intensity threshold due to overlap contributions in the multiphase region, consistent with the known difficulty of deconvoluting low-intensity reflections in two-population patterns. The test for Phase B is decisive: if Phase B were a disordered $Pm\text{-}\bar{3}m$ or $Fm\text{-}\bar{3}m$ form of Mg_2FeVO_6, its (310) reflection at $2\theta = 28.023°$ would carry zero intensity. It is observed at $I = 50.73\%$, the 4th most intense peak in the entire pattern. Phase B is therefore an ordered $Ia\text{-}\bar{3}d$ double perovskite-related structure, not a disordered impurity.

Quantitative phase fractions were determined from the Le Bail refinement using the Hill–Howard ZMV integrated-area method, with Z the number of formula units per cell, M the molecular mass, and V the refined unit-cell volume. The analysis yields: Phase A 51.7 ± 4.0 wt% (49.9 vol.%, 51.8 mol%), Phase B 42.2 ± 8.0 wt% (45.0 vol.%, 42.3 mol%), and $Mg_2V_2O_7$ 6.1 ± 1.5 wt% (5.1 vol.%, 5.9 mol%). The combined Mg_2FeVO_6 content (Phase A + Phase B) is 93.9 ± 9.0 wt%, establishing that the sample is a predominantly single-compound material with a minor vanadate impurity. The $Mg_2V_2O_7$ impurity at 6.1 wt% reflects incomplete V^{5+} incorporation into the double perovskite-related structure during the 900 °C anneal. The calculated densities from refined parameters are 3.274 g cm^{-3} (Phase A), 2.969 g cm^{-3} (Phase B), and 3.783 g cm^{-3} ($Mg_2V_2O_7$), with $Z = 8$ for both $Ia\text{-}\bar{3}d$ phases and $Z = 2$ for $Mg_2V_2O_7$.

Complete peak assignment from Le Bail profile fitting is available at Table S2 (in SI files). Phase identification against standard reference data confirms the three-phase assignment. Six peaks in the pattern are assigned to the secondary phase $Mg_2V_2O_7$ (triclinic $P\text{-}\bar{1}$, ICDD 00-029-0877). The peak at $2\theta = 17.36°$ (d = 5.104 Å) matches the d = 5.064 Å reference line of $Mg_2V_2O_7$ within $\Delta = +0.78\%$; critically, this reflection is also where the (200) reflection of $Ia\text{-}\bar{3}d$ would fall, but (200) is forbidden in $Ia\text{-}\bar{3}d$ ($h00$ requires $h = 4n$; $h = 2$ fails this condition), so the peak is unambiguously assigned to $Mg_2V_2O_7$. Additional $Mg_2V_2O_7$ peaks at 2θ = 28.99°, 29.49°, 30.17°, 32.49°, and 43.29° match ICDD reference positions within ±0.4%. The peak at 24.17° is a coincident overlap of the Phase B (220) fundamental reflection (d_{calc} = 3.679 Å) with the $Mg_2V_2O_7$ d = 3.679 Å reference line; the contribution from each phase was assigned equally in the quantitative analysis. All assigned $Mg_2V_2O_7$ peaks are consistent with ICDD positions and are not predicted by any $Ia\text{-}\bar{3}d$ reflection. Hematite Fe_2O_3 (ICDD 00-033-0664, $R\text{-}\bar{3}c$) cannot be confirmed or excluded, as all its reference lines overlap with $Ia\text{-}\bar{3}d$ reflections within experimental tolerance; no unambiguous diagnostic peak is present.

The physical origin of the two-population cell-parameter distribution is consistent with B-site oxidation-state heterogeneity between crystallite populations formed during sol–gel crystallization at 900 °C. Substitution of Fe^{2+} (r = 0.780 Å) for Fe^{3+} (r = 0.645 Å), or V^{4+} (r = 0.580 Å) for V^{5+} (r = 0.540 Å), in a minority of crystallites would expand the unit cell in the manner observed, corresponding to a compositional variation of $\Delta x \approx \pm 0.05$ in $Mg_2Fe_{1+x}V_{1-x}O_6$ as expected from incomplete cation mixing at this temperature. The Mg^{2+} cation, undersized for the 24 d Wyckoff A-site cavity in $Ia\text{-}\bar{3}d$, produces local lattice strain that manifests as this two-population cell-parameter spread ($\Delta a/a = 1.81\%$) rather than as a long-range symmetry-lowering phase transition, which is consistent with the complete absence of peak splitting or superlattice reflections attributable to octahedral tilting.

Table 2 summarizes the refined crystallographic parameters for all three identified phases. The refined lattice parameters for Phase A and Phase B are $a_0 = 10.098 \pm 0.025$ Å $a_0 = 10.402 \pm 0.004$ Å respectively. The lattice parameter value for Phase A is in good agreement for $Ia\text{-}\bar{3}d$ $A_2BB'O_6$ double perovskites with Mg^{2+} on the A-site. The calculated subcell parameters, are consistent with the $A_2BB'O_6$ stoichiometry. The two populations are different by $\Delta a/a = 3.01\%$, with Phase B having the bigger cell. Both populations exhibit identical $Ia\text{-}\bar{3}d$ symmetry and possess B-site ordering reflections, thereby validating that Phase B is neither a disordered impurity nor a separate compound, but rather a second ordered $Ia\text{-}\bar{3}d$ crystallite ensemble of the same material.

Structural contrast with Ba_2FeVO_6 and the effect of A-site cation substitution: The substitution of Ba^{2+} with Mg^{2+} in the A_2FeVO_6 system produces dramatic structural differences despite similar sol–gel preparation methods. Ba_2FeVO_6 synthesized from mixed $BaVO_3/BaFeO_3$ sols with citric acid complexation crystallizes in hexagonal $R\text{-}3c$ when sintered at 900 °C, with characteristic XRD reflections at $2\theta = 27.52°$ and $30.96°$ (ref. 7, Fig. 2). These peaks correspond to the hexagonal close-packed AO_3 layer structure favored by large A-site cations. The tolerance factor for Ba_2FeVO_6 ($t \approx 1.08$, calculated using $r\text{Ba} = 1.61$ Å, CN = 12) exceeds unity, destabilizing the cubic perovskite framework in favor of face-sharing octahedral dimers.

Mg_2FeVO_6 prepared by the analogous sol–gel route with a higher citric acid: metal ratio (3 : 1) and slightly higher drying temperature (120 °C *vs.* 100 °C) exhibits entirely different XRD characteristics. The hexagonal reflections characteristic of $R\text{-}3c$ Ba_2FeVO_6, identified from the reference pattern at Cu Kα radiation ($\lambda = 1.5419$ Å) at $2\theta = 27.52°$ and $30.96°$, are absent in the present pattern. Instead, the pattern shows intense superstructure reflections at $2\theta = 27.07°$ (310, $I = 94.7\%$) and $33.19°$ (321, $I = 67.6\%$), which are symmetry-forbidden in both hexagonal $R\text{-}3c$ and disordered cubic $Pm\text{-}\bar{3}m$. These peaks confirm cubic $Ia\text{-}\bar{3}d$ symmetry with rock-salt B-site ordering, stabilized by the smaller Mg^{2+} cation ($t = 0.862$).

The crystallite size at 900 °C differs substantially: 44.7 nm for Ba_2FeVO_6 *versus* 26.1 nm for Mg_2FeVO_6. This 42% reduction suggests slower cation diffusion and grain growth limitation in the Mg system due to stronger citric acid complexation (3 : 1 ratio *vs.* unstated) or the smaller Mg^{2+} ionic radius requiring higher energy for lattice incorporation. Impurity profiles also reflect A-site chemistry: Ba_2FeVO_6 synthesized at lower temperatures (500–700 °C) shows $BaCO_3$, $Ba_2V_2O_7$, and Fe_2O_3 intermediates from precursor decomposition and atmospheric CO_2 reactivity, while Mg_2FeVO_6 at 900 °C exhibits only $Mg_2V_2O_7$ as a secondary phase with no carbonate formation, consistent with the thermal stability of magnesium acetate *versus* barium acetate precursors.

The quantitative ordering indicator $\Sigma I(\text{ord})/\Sigma I(\text{fund}) = 1.59$ in Mg_2FeVO_6 confirms substantial long-range Fe/V ordering within the $Ia\text{-}\bar{3}d$ framework. The available literature on Mg_2FeVO_6 does not report a quantitative ordering indicator of the type employed here. The hexagonal $R\text{-}3c$ structure adopted by Ba_2FeVO_6 (ref. 7 and 20) does not support the rock-salt B-site ordering characteristic of $Ia\text{-}\bar{3}d$; any B-site arrangement present in $R\text{-}3c$ is geometrically distinct from the alternating octahedral site occupancy confirmed here. This structural switch, from hexagonal disordered to cubic ordered, demonstrates that A-site cation size is the dominant factor controlling both symmetry and B-site arrangement in the A_2FeVO_6 family, overriding the common influence of synthesis methodology.

The Goldschmidt tolerance factor provides structural context for these observations. Using Shannon ionic radii[21] with the B-site averaged over equal Fe and V occupancy, determined as $r\text{B(avg)} = (r\text{Fe}^{3+} + r\text{V}^{5+})/2 = (0.645 + 0.540)/2 = 0.5925$ Å, the calculation requires a coordination number for Mg^{2+} at the A-site. The CN = 6 value ($r = 0.720$ Å, $t = 0.752$) corresponds to

Table 2 Refined crystallographic parameters from Le Bail profile fitting (17–85°, Cu Kα, $\lambda = 1.5419$ Å). Reliability factors: $R_p = 31.77\%$, $R_{wp} = 41.12\%$, $R_{exp} = 69.08\%$, $\chi^2 = 0.354$. $Mg_2V_2O_7$ triclinic parameters from ICDD 00-029-0877; angles α, β, γ not independently refined. Lattice parameters for Mg_2FeVO_6 phases from Le Bail refinement; geometric indexing values (Phase A: 10.128 ± 0.121 Å, Phase B: 10.311 ± 0.159 Å) served as starting values

Parameter	Phase A—Mg_2FeVO_6	Phase B—Mg_2FeVO_6	$Mg_2V_2O_7$
Space group (No.)	$Ia\text{-}\bar{3}d$	$Ia\text{-}\bar{3}d$	$P\text{-}\bar{1}$ (2)
Lattice parameter a (Å)	10.098 ± 0.025	10.402 ± 0.004	$a = 6.087$, $b = 8.463$, $c = 4.575$
Unit-cell volume V (Å^3)	1029.7	1125.6	230.4
$a_{sub} = a/2$ (Å)	5.049	5.201	—
$\Delta A/a$ (%)	—	3.01	—
Z	8	8	2
M (g mol^{-1})	272.03	272.03	262.43
ρ_{calc} (g cm^{-3})	3.274	2.969	3.783
Weight fraction (wt%)	51.7 ± 4	42.2 ± 8	6.1 ± 1.5
Volume fraction (vol.%)	49.9	45.0	5.1
Mole fraction (mol%)	51.8	42.3	5.9

the B-site octahedral environment and is internally inconsistent with the perovskite formula; CN = 8 ($r = 0.890$ Å, $t = 0.813$) is appropriate only when the A-site cation is too small to fill the 12-coordinate cavity. The standard convention for $A_2BB'O_6$ double perovskites uses CN = 12, following Woodward (1997)[22] and King & Woodward (2010).[23] The CN = 12 value is not tabulated by Shannon (1976)[21] for Mg^{2+}, whose entries extend only to CN = 8; the value used here ($r = 1.03$ Å) is an effective radius estimated by linear extrapolation of the coordination-number trend observed for comparable alkaline-earth divalent cations with full CN = 4–12 data in Shannon (1976),[21] specifically Ca^{2+} and Sr^{2+}, for which the radius increases systematically and near-linearly with coordination number across the full range. The structural assignment rests on the experimental XRD evidence, not on this extrapolated value.

$$t = \frac{r\mathrm{Mg} + r\mathrm{O}}{\sqrt{2}\left(\frac{1}{2}(r\mathrm{Fe} + r\mathrm{V}) + r\mathrm{O}\right)} = 0.862$$

The value $t = 0.862$ falls below the empirical cubic stability threshold of ~0.89–0.90 derived for simple ABO_3 perovskites; however, this threshold does not constitute a physical law and is known to be relaxed for $A_2BB'O_6$ double perovskites in *Ia*-$\bar{3}$*d*.[22,24,25] The lower bound of the *Ia*-$\bar{3}$*d* cubic stability field for $A_2BB'O_6$ double perovskites is known to extend below $t = 0.89$, as documented across the comprehensive survey of approximately one thousand $A_2BB'O_6$ compounds by Vasala & Karppinen.[24] Monoclinic $P2_1/n$ distortion is reported for compounds with $t < 0.85$ in that same survey. With $t = 0.862$ falling between these bounds, the present compound lies within the transitional region where the Goldschmidt factor alone is not predictive, and the experiment is decisive: the XRD pattern shows no evidence of peak splitting, octahedral tilting reflections, or any violation of cubic *Ia*-$\bar{3}$*d* extinction rules across all 22 Mg_2FeVO_6 peaks. The contrast with Ba_2FeVO_6 (ref. 7 and 20) is instructive: the larger Ba^{2+} ($r = 1.61$ Å, CN = 12, $t = 1.078$) places the Ba analogue above the ideal cubic value of $t = 1.0$, where the hexagonal *R*3*c* structure is favored over the cubic double perovskite arrangement, as confirmed by Pei *et al.*[20] Reducing the A-site from Ba^{2+} to Mg^{2+} drives t from 1.078 to 0.862, shifting the compound out of the hexagonal stability field and into the *Ia*-$\bar{3}$*d* cubic double perovskite-related field indicated experimentally here. Sahu *et al.*[9] report $t = 0.76$ using a modified double perovskite tolerance factor with A-site averaging, though the specific ionic radii and coordination numbers employed are not stated. Back-calculation from their reported value implies $r\mathrm{Mg} \approx 0.74$ Å, consistent with octahedral CN = 6 coordination. Application of the standard CN = 12 convention for A-site cations in $A_2BB'O_6$ double perovskites,[22,24,25] using the extrapolated value $r\mathrm{Mg} = 1.03$ Å, yields $t = 0.862$ in both formulations, consistent with the experimentally observed cubic *Ia*-$\bar{3}$*d* symmetry confirmed by both studies.

The Le Bail refinement confirms that the (400) reflection of Phase A at $2\theta = 35.622°$ is the strongest non-overlapping fundamental reflection in the pattern, with no contribution from Phase B or $Mg_2V_2O_7$ predicted at this position, making it the optimal and unambiguous choice for single-peak crystallite size analysis. Crystallite size may be estimated using the Scherrer equation applied to an isolated reflection. A 5-point moving average was applied to the raw diffraction data prior to peak profile fitting. Crystallite size was estimated by pseudo-Voigt profile fitting of the strongest non-overlapping fundamental reflection, (400), at $2\theta = 35.622°$ (Fig. S1, SI). The fit yielded a center position of $2\theta° = 35.648 \pm 0.001°$, FWHM $\beta = 0.317 \pm 0.005°$ (0.005523 rad), and $R^2 = 0.995$. Applying the Scherrer equation $D = K\lambda/(\beta \cos\theta)$ with $K = 0.89$, $\lambda = 1.5419$ Å, and β in radians yields a crystallite size value (D) = 26.1 nm. This estimate is derived from a single isolated reflection and does not represent a mean value averaged across multiple peaks; multi-peak analysis is precluded by the two-population lattice parameter distribution, which prevents unambiguous assignment of broadening contributions on a peak-by-peak basis. Williamson–Hall analysis was not performed for the same reason; detailed line broadening analysis is reserved for future work.

The structural characteristics of Mg_2FeVO_6 ceramics demonstrate marked synthesis dependence when compared with the solid-state route reported by Sahu *et al.*[9] Their calcination at 1050 °C and sintering at 1100 °C produced a three-phase mixture comprising cubic *P*432 ($a = 8.38$ Å, 31.65%), cubic *Ia*-$\bar{3}$*d* ($a = 12.43$ Å, 43.92%), and orthorhombic *Pnma* ($a = 9.791$, $b = 3.687$, $c = 12.727$ Å, 24.43%) (ref. 9, Table 1). The dominant *Ia*-$\bar{3}$*d* phase reported by Sahu *et al.* carries $a = 12.43$ Å, which the present authors note exceeds the typical $A_2BB'O_6$ double perovskite range ($a \approx 10$ Å) and falls within the lattice parameter range characteristic of garnet-type structures ($a \approx$ 12–13 Å); Sahu *et al.* assign this phase as double perovskite, and the discrepancy in cell parameter merits further structural investigation. The present sol–gel synthesis at 900 °C yields cubic *Ia*-$\bar{3}$*d* with $a = 10.128$ Å (Phase A) and $a = 10.311$ Å (Phase B), consistent with established double perovskite-related stoichiometry. Notably, the cell parameters differ substantially from the *P*432 ($a = 8.38$ Å) and large-cell *Ia*-$\bar{3}$*d* ($a = 12.43$ Å) phases reported by Sahu *et al.*, and no orthorhombic *Pnma* distortion is observed.

Crystallite size measurements reflect both methodology and phase purity differences. Sahu *et al.* report 38.9 nm (Scherrer) and 54.2 nm (Williamson–Hall) from their multiphase mixture with microstrain $\varepsilon = 0.000206$. The present work yields 26.1 nm from Scherrer analysis of the isolated (400) reflection. This lower value is consistent with the 200 °C lower maximum processing temperature, though direct comparison is complicated by differences in phase purity and the inability to perform multi-peak Williamson–Hall analysis due to the two-population lattice parameter distribution in the present sample. Sahu *et al.*[9] additionally, report SEM grain sizes of 191.5 nm with an agglomeration ratio of 5; comparable microstructural data were not obtained in the present study. The present study, employing sol–gel synthesis at 900 °C, yields a cubic *Ia*-$\bar{3}$*d* double perovskite-related structure ($a = 10.128$ Å) as the dominant product with no evidence of garnet or *Pnma* phases, demonstrating the critical role of synthesis route in determining phase formation in magnesium iron vanadate ceramics. Detailed structural refinement including B-site order parameter quantification and M–O bond length determination is identified as a priority for future work.

3.2 FTIR analysis

The Fourier transform infrared (FTIR) spectroscopy measurement has been carried out to confirm the presence of functional groups in addition to chemical bonding of Mg_2FeVO_6. The FTIR spectrum provided in Fig. 3 reveals multiple characteristic absorption bands corresponding to hydroxyl groups, adsorbed water, and metal–oxygen vibrations, consistent with the phase composition identified by XRD. The broad adsorption band centered at ~3430 cm^{-1} is attributed to O–H stretching vibrations of surface hydroxyl groups and physisorbed water molecules. A separate weak adsorption at ~2922 cm^{-1} is assigned to C–H stretching of residual organic species from the sol–gel synthesis process. The O–H bending vibration of adsorbed water molecules appears at ~1620 cm^{-1}, and its presence confirms the hydrophilic character of Mg_2FeVO_6. The weak band at ~1400 cm^{-1} is attributed to carbonate species formed by interaction of surface hydroxyl groups with atmospheric CO_2. The surface hydroxyl groups evidenced by the 3430 and 1620 cm^{-1} bands provide the primary active sites for water molecule adsorption, directly supporting the protonic conduction mechanism proposed for the humidity sensing response.

In the low-wavenumber region, the band at ~990 cm^{-1} is attributed to V–O stretching vibrations consistent with vanadium-oxygen bonding in the synthesized ceramic. The band at ~810 cm^{-1} corresponds to M–O stretching vibrations of the BO_6 octahedra (Fe/V), consistent with Fe^{3+} and V^{5+} in octahedral coordination.[26] The band at ~665 cm^{-1} is assigned to B–O–B bending vibrations, while the band at ~523 cm^{-1} is attributed to O–V–O bending modes. The band at ~435 cm^{-1} is attributed to combined O–Fe–O bending and Mg–O stretching vibrations, consistent with assignments reported for iron and magnesium oxide systems.[27–29] The metal–oxygen vibrational bands identified in the FTIR spectrum are consistent with the *Ia*-$\bar{3}$*d* cubic double perovskite-related structure established by XRD. The presence of distinct VO_6 and FeO_6 octahedral stretching modes confirms local B-site occupancy by vanadium and iron, while the sharp, well-resolved character of the metal–oxygen bands in the fingerprint region is consistent with the high crystallinity confirmed by XRD.

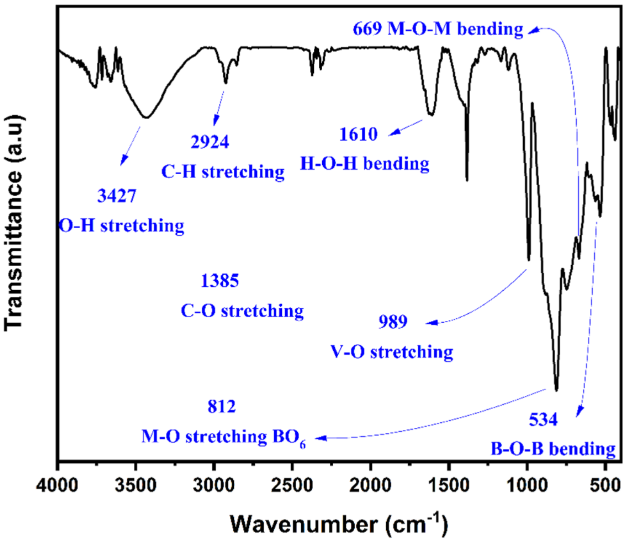

Fig. 3 The FTIR transmittance spectrum of Mg_2FeVO_6 ceramic in the spectral range from 400 cm^{-1} to 4000 cm^{-1}, showing characteristic bands of surface hydroxyl groups, physisorbed water, and metal–oxygen vibrations indicating perovskite framework formation.

3.3 Surface morphology

The morphology of the prepared Mg_2FeVO_6 ceramic is demonstrated in Fig. 4. The SEM image at low magnification (25 000×) demonstrated particles distributed across the surface, with small particles forming dense clusters in some areas and other larger isolated particles, likely representing agglomerates of multiple crystallites. The particles have well-defined shapes with sizes ranging from small nanoparticles (40–80 nm) to larger agglomerates (up to several hundred nanometers). Small particles forming dense clusters in some areas, with cluster dimensions appearing to reach several hundred nanometers, consistent with the agglomeration tendency indicated by DLS measurements. The sample shows good densification, evidenced by the absence of large cracks or macroscopic pores, and the particles look solid with no holes inside them. Individual particle size analysis was performed from the high-magnification SEM image (100 000×), revealing more detailed morphology, showing particles with spherical to slightly irregular shapes. No abnormal morphologies are observed in the SEM images. No apparent pores or voids between the particles. The edges or grain boundaries between particles are clearly visible. Particle size analysis from the high-magnification image shows an average particle size of ~75.6 nm, while the crystallite size obtained from XRD analysis is ~26.1 nm. The relative size SEM/XRD ratio is ~2.9, indicating that individual particles are polycrystalline, each comprising multiple crystallites. The dense and continuous microstructure supports stable electrical contact paths during humidity sensing, though the limited porosity restricts water vapor diffusion to interior adsorption sites, contributing to the observed response time.[30]

3.4 Zeta potential

The electrokinetic properties of the synthesized sample were evaluated using zeta potential measurements (Fig. 5). The measured zeta potential of −19 mV confirms the presence of negative surface charges, attributed to surface hydroxyl groups consistent with the O–H stretching band at ~3430 cm^{-1} identified by FTIR analysis.[31] The magnitude of −19 mV falls within the transitional stability region, indicating moderate electrostatic repulsion between particles, consistent with the agglomeration tendency observed in DLS measurements. The negatively charged surface hydroxyl groups act as active adsorption sites for water molecules,[6] facilitating their dissociation into hydronium ions (H_3O^+) and hydroxide ions. These surface-accessible active sites support the Grotthuss proton-

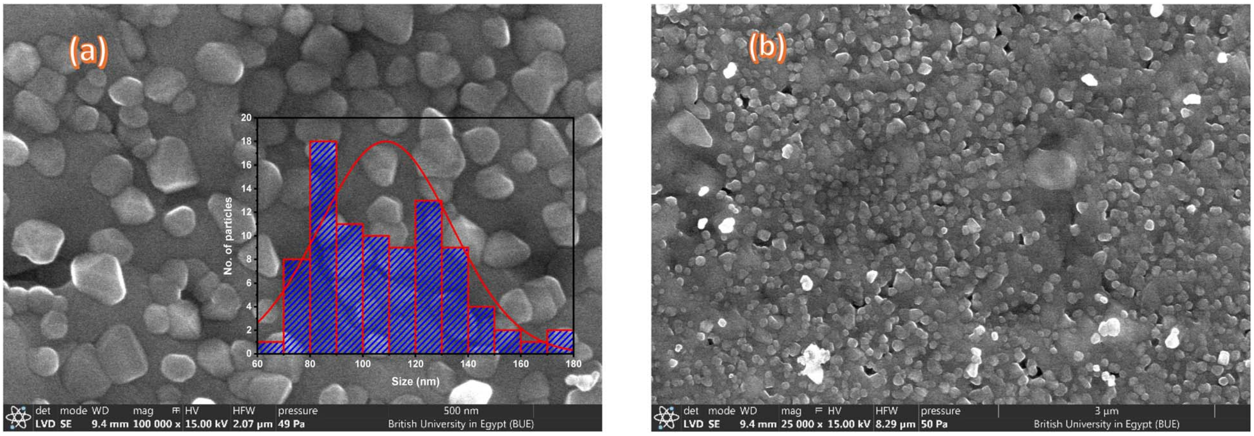

Fig. 4 The SEM images of Mg_2FeVO_6 at different magnifications: (a) 100 000× magnification with inset showing particle size distribution (n = 50), and (b) 25 000× magnification showing detailed morphology.

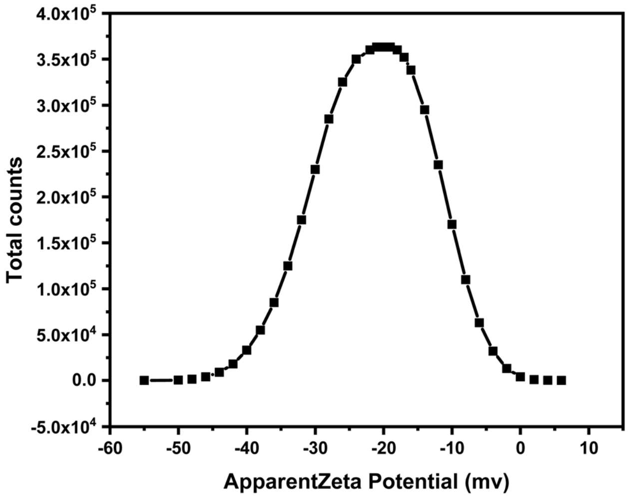

Fig. 5 Zeta potential distribution of Mg_2FeVO_6.

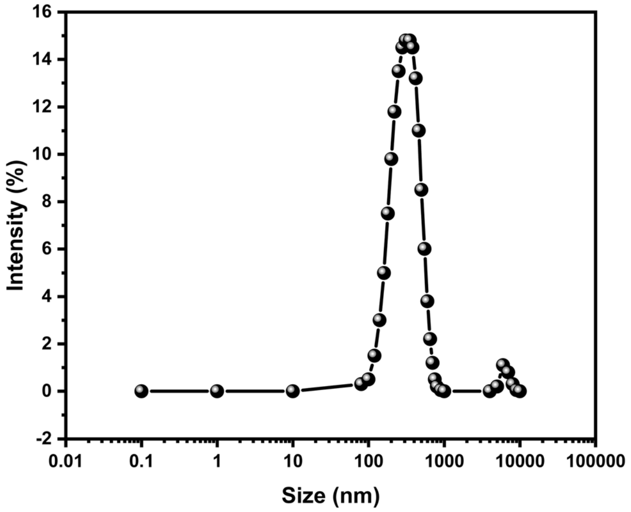

Fig. 6 Particle size distribution of Mg_2FeVO_6 measured using the DLS technique.

hopping mechanism, in which H_3O^+ ions serve as the primary charge carriers, enabling electrical conductivity modulation in response to varying relative humidity.

3.5 Particle size distribution by DLS

The dynamic light scattering technique was used to measure the diameter of the synthesized sample, as shown in Fig. 6. DLS measurements were performed at 25 °C in deionized water (pH ≈ 6–7) at a concentration of 0.12 mg mL^{-1} following bath sonication. The *Z*-average hydrodynamic diameter was 358.1 nm with a PDI of 0.382, indicating a moderately polydisperse size distribution. The intensity-weighted size distribution revealed a primary peak centered at 306.3 nm, accounting for 98.9% of scattered intensity, while a minor secondary peak at 5560 nm reflects a small fraction of larger aggregates. The *Z*-average exceeds the primary peak position as it incorporates contributions from all populations. The hydrodynamic diameter (306.3 nm) is approximately four times the average particle size measured by SEM (75.6 nm). This discrepancy reflects two contributions: the hydrodynamic diameter includes the solvation layer and adsorbed molecules surrounding each particle, and more significantly, particles tend to agglomerate in aqueous suspension. The low zeta potential measured for this sample [−19 mV] is consistent with weak inter-particle electrostatic repulsion, favoring agglomeration in suspension. In contrast, SEM measures dry, individually resolved particles. Together, the crystallite size (XRD: 26.1 nm), particle size (SEM: 75.6 nm), and hydrodynamic diameter (DLS: 306.3 nm) reflect three distinct length scales: individual crystallites, polycrystalline particles, and suspension aggregates, respectively.[32]

3.6 Humidity sensing performance

The dielectric properties of the Mg_2FeVO_6 have been studied under dry conditions by Sahu *et al.*; however, the effect of varying humidity levels on the dielectric properties has not been investigated. Hence, the humidity sensing performance of

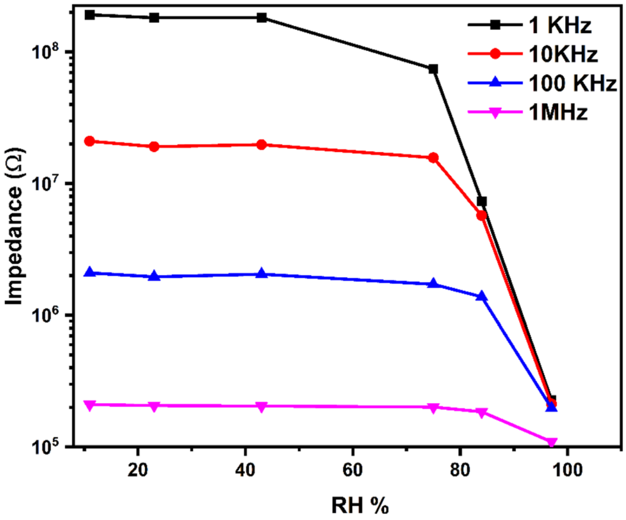

Fig. 7 The impedance variation as a function of humidity levels at different testing frequencies.

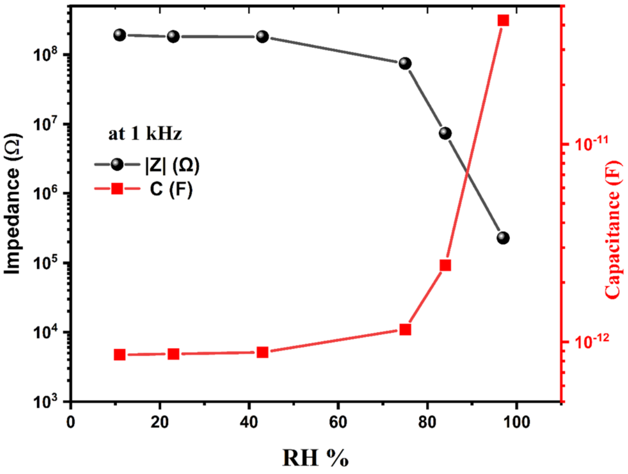

Fig. 8 Capacitance and impedance as a function of RH at 1 kHz.

Mg_2FeVO_6 is reported here for the first time. The humidity response of the sensor at different testing frequencies is shown in Fig. 7. The impedance value decreases as the RH level increases for all applied frequencies, while the largest change was achieved at 1 kHz.[5] The investigated sensor revealed a dependence on the applied AC frequency. This is a common phenomenon for all humidity sensors. It is well known that the water molecules are polar; when adsorbed on the surface of the humidity sensor, they try to follow the fluctuation of the applied AC signal. At low frequency, the water molecules have enough time to align with the electric field, while at higher frequencies, the adsorbed water molecules cannot physically orient themselves to follow the rapidly oscillating AC field; this in turn results in reducing the impedance variation at high frequencies. The above performed test is essential to determine the optimum or best testing conditions, especially the applied AC frequency. The sensor response was further evaluated by measuring capacitance at different RH levels. The capacitance of the fabricated sensor was measured as a function of RH. The impedance and capacitance variation as a function of RH at 1 kHz is shown in Fig. 8. The capacitance of the fabricated sensor increases as the humidity level increases,[6] as shown in Fig. 8. The capacitance demonstrated a non-linear dependence on RH. The capacitance increases slowly for low humidity levels up to 43% RH. Beyond 43% RH, a rapid increase in capacitance was observed, where the capacitance increased by orders of magnitude.[33]

The same trend was also recognized for impedance, where the impedance decreases as the RH increases. Sensitivity is an interesting parameter that evaluates the performance of the humidity sensors. The normalized response or the sensitivity (S in % RH^{-1}) for both impedance (Z) and capacitance (C) over the full humidity range from 11% RH to 97% RH can be calculated from the following equation:[34]

$$S = [(Y_{\max} - Y_{\min})/Y_{\min}] \times (100/\Delta \mathrm{RH}) \qquad (6)$$

where $Y_{\min}$ and $Y_{\max}$ represent the impedance/capacitance value at 11% RH and 97% RH levels, respectively. ΔRH is the difference between maximum (97% RH) and minimum (11% RH) RH levels and it is equal to =97–11 = 86. The calculated normalized sensitivity for both impedance and capacitance is shown in Table 3.

It is worth mentioning that the negative sign of impedance sensitivity comes from the inverse relationship between impedance and RH, while the positive sign arises from the direct proportion between capacitance and relative humidity. This sign is directional sign not related to the sensing mechanism. So, for comparison the absolute value of the impedance sensitivity $|-1.16| = 1.16\%\ \mathrm{RH}^{-1}$ will be used throughout the text. As can be seen from Table 3, capacitance is a more sensitive parameter than impedance; its normalized sensitivity is about 48 times greater than that of impedance.

The repeatability test (impedance and capacitance) for the fabricated sensor was measured between 11% and 75% for four cycles, as shown in Fig. 9. The repeatability test for both impedance and capacitance revealed consistent and reversible

Table 3 The normalized sensitivity for both impedance and capacitance

Parameter	Minimum value (11% RH)	Maximum value (97% RH)	Absolute change (ΔY)	Sensitivity (% RH^{-1})
Impedance	191.38 MΩ	227.15 kΩ	191.15 MΩ	1.16
Capacitance	0.86 pF	42.31 pF	41.45 pF	56.04

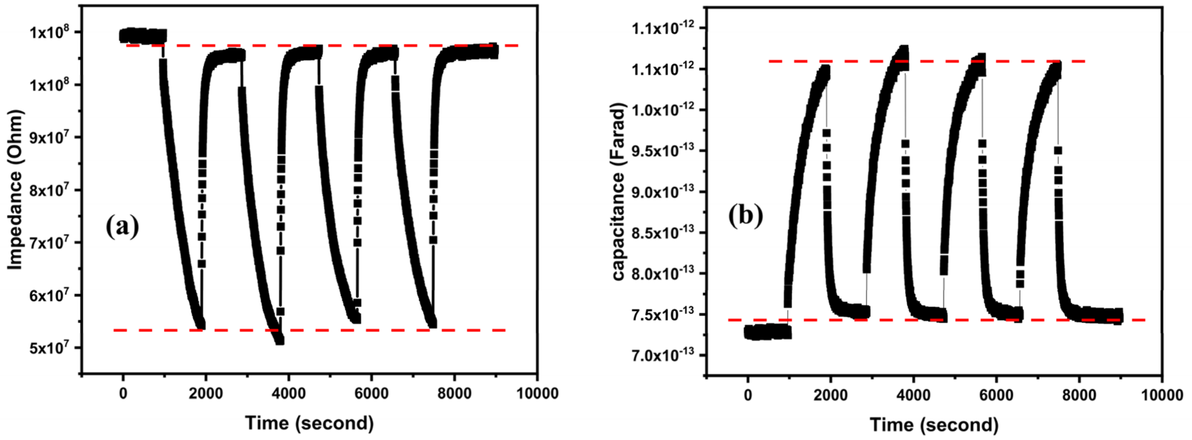

Fig. 9 The repeatability of the tested sensor, (a) impedance and (b) capacitance.

behavior that confirmed the ability of the sensor to track humidity changes repeatedly.[35] A low downward drift for impedance and upward drift for capacitance were observed; however, the shape and the span of the cycles for both impedance and capacitance remain relatively consistent, suggesting that the sensitivity and response mechanism are stable.

Response time is defined as the time required by the sensor to reach 90% of the total change from dry to wet conditions, while recovery time is the time taken by the sensor to reach 90% of its baseline value. The calculated response and recovery times (Fig. 10) were found to be 760 seconds and 25 seconds, respectively. The prolonged response time is linked to the limited adsorption process of water molecules, which could be attributable to the densely packed, low-porosity microstructure confirmed by SEM, which restricts water vapor diffusion through the material regardless of surface reactivity.[36,37] The SEM image of Fig. 4 reveals a compact packed sensing layer composed of aggregated particles with limited inter-particle porosity. In a porous material, water vapor can access adsorption sites throughout the open pore channels, hence the diffusion path length is efficiently shortened by the connected void network. In the present Mg_2FeVO_6, the dense, low-porosity morphology means that water vapor molecules must cross a complex path through narrow inter-particle gaps to reach interior adsorption sites. This in turn increases the effective diffusion path length relative to the geometric layer thickness, reducing the rate at which vapor equilibrates with the bulk of the sensing layer. This microstructural bottleneck is the primary physical origin of the 760 s response time, and it is consistent with the fast recovery time of 25 s. During desorption process, water molecules near the surface are released directly into the lower-humidity environment without requiring inward diffusion, so the rate-limiting step is absent and desorption proceeds rapidly. The surface hydroxyl groups identified by zeta potential measurements confirm adequate adsorption site density; the rate-limiting step is therefore mass transport through the pore network, not surface chemistry.

The rapid recovery time relative to the response time reflects an asymmetry in adsorption and desorption kinetics: while water vapor adsorption requires diffusion through the dense microstructure to reach interior surface sites, desorption of surface-bound water proceeds readily once the humidity gradient is reversed, as molecules near the surface are released without the same diffusion constraint. This kinetic asymmetry is consistent with the dense, low-porosity morphology identified by SEM and confirms that the rate-limiting step is inward vapor diffusion rather than the surface interaction itself. The slow response of the Mg_2FeVO_6 based humidity sensor can be attributed to various factors that control the transport and adsorption kinetics of water molecules through the sensing layer. These factors are surface area, active sites, film thickness, diffusion path length, pore structure, agglomeration, and surface chemistry.[36,38] The density of the active sites is proportional to the specific surface area. The DLS and SEM investigations reveal that Mg_2FeVO_6 has a particle size of 306 nm to 5.6 μm. These larger particles reduce the effective surface area required for water adsorption. The water molecules need to be diffused through the entire thickness of the humidity sensor to interact with active sites at the bottom of the sensing layer, where the thicker sensing layer offers more adsorption sites; however, this will increase the response time due to extended

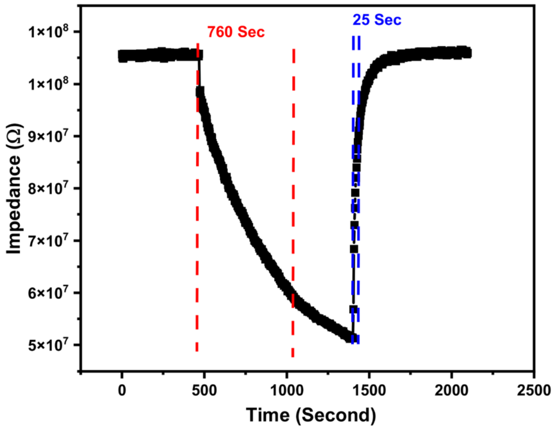

Fig. 10 The response and recovery times of the fabricated sensor.

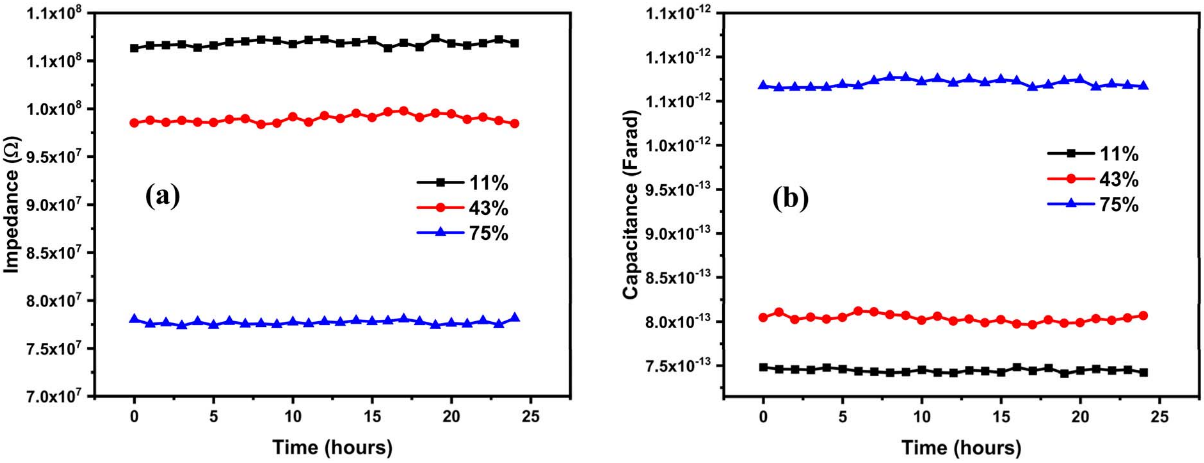

Fig. 11 Short-term stability of the studied sensors at different RH levels: (a) impedance and (b) capacitance.

diffusion paths. One of the most important factors is the density and distribution of active sites on the surface of the sensing layer. Zeta potential measurements (−19 mV) confirmed the presence of hydroxyl group, however these groups could not be uniformly distributed over the surface of the Mg_2FeVO_6 sensing material, hence chemisorption kinetics at low RH can propagate into longer overall response times. In conclusion, the response time can be formulated as a combination of different processes given by the following equation:

$$\tau_{\text{total}} = \tau_{\text{diffusion}} + \tau_{\text{chemisorption}} + \tau_{\text{physisorption}} + \tau_{\text{film formation}}$$

In our reported sensor, the dominant contribution factor could be diffusion-limited transport through the aggregated and porous film structure. The fabricated sensor is suitable for specific applications where rapid cycling is not critical, but its long-term stability and accuracy are mandatory. In some applications like monitoring climate changes, the humidity changes gradually over hours or days, rather than seconds. Museums, archive preservation, building automation, and HVAC systems are designed to maintain stable environmental conditions where humidity fluctuations occur slowly. The proposed sensor provides high sensitivity without noticeable drift that ensures reliable operation over months.

Short-term stability of the sensor has been measured for 25 hours at 11%, 43%, and 75% RH, as shown in Fig. 11. The studied sensor maintained a stable output across all tested RH levels. The short-term stability of the studied sensor revealed excellent stability across all tested RH levels. The short-term stability indicated that the sensor responses are consistent over time, exhibiting a flat line for each RH level without any significant random noise, short-term degradation, or drift. The obtained results of short-term stability confirmed that the studied sensing materials are reliable and do not require frequent recalibration.

Table 4 compares the humidity sensing performance of Mg_2FeVO_6 with selected perovskite-based sensors reported in the literature. Doped $LaFeO_3$ perovskite achieves a 2094% capacitance response with a response time of 4.4 s and recovery time of 1.4 s, attributed to Ti-induced porosity and high specific surface area.[39] Cs_2SnCl_6-based impedance sensors show an impedance change of 2.2×10^6 with a response time of 0.8 s,[40] while Cs_2SnCl_6/GO composites achieve an impedance change of

Table 4 Comparison of humidity sensing performance of Mg_2FeVO_6 with selected perovskite-based sensors. Sensitivity values are reported as normalized responses per % RH where available. Response and recovery times are defined as the time to reach 90% of the total signal change

Material	RH range (%)	Sensitivity	Response/recovery (s)	Notable features	Ref.
Mg_2FeVO_6	11–97	Capacitance: 56.04% RH^{-1}	760/25	First report of humidity-dependent dielectric and electrical properties for this material	This work
LaFe0.925$Ti_{0.075}O_3$	11–97	2094% capacitance response	4.4/1.4	High porosity, less than 1% hysteresis, 28-days stability	39
Cs_2SnCl_6	11–95	2.2×10^6 impedance change	0.8/5.4	Reversible, stable	40
Cs_2SnCl_6/GO	11–97	6.5×10^6 impedance change	0.8/1.9	More than 240 days stability	41
$CsPb_2Br_5/BaTiO_3$	25–95	$\Delta C/C_0$ up to 4,500,000% at 0.5 kHz	2/2	Highest signal variation reported for breath monitoring	42

6.5×10^6 with stability exceeding 240 days.[41] $CsPb_2Br_5/BaTiO_3$ demonstrates the highest electrical signal variation reported for breath-scale humidity sensing, operating through water-induced interfacial polarization.[42]

Mg_2FeVO_6 achieves a capacitance sensitivity of 56.04% RH^{-1}across the full 11% to 97% RH range, which is competitive with impedance-type perovskite sensors. The response time of 760 s is longer than fast-cycling sensors. The surface hydroxyl groups confirmed by zeta potential measurements confirm adequate surface reactivity. The rate-limiting step is mass transport through the sensing layer, not surface chemistry. Morphology optimization strategies such as porosity engineering are identified as the primary direction for improving response kinetics in future work.

3.7 Humidity sensing mechanism

The humidity sensing mechanism is analyzed using phase angle and complex impedance spectroscopy. The phase angle is a measure of the phase shift between the AC voltage and AC current across the sensor. The phase angle of most humidity sensors (Fig. 12a) is between 0° and 90° because they behave as a combination of a resistor and a capacitor. The phase angle at low and mid humidity levels is approximately 90°, indicating that the sensor behaves like an ideal capacitor. At low to mid-RH levels, the phase angle approaches −90°, indicating predominantly capacitive behavior. At this stage, few water molecules are adsorbed on the sensor surface, leaving the material with negligible ionic conductivity and very high electrical resistance, with the response dominated by dielectric displacement current rather than resistive conduction.[6] Additionally, the phase angle curves overlapped and were indistinguishable, meaning that the phase angle is insensitive to changes in humidity up to 43%. The Nyquist plot of Fig. 12b revealed the following: At low RH, the resistance is sufficiently large for the semicircle diameter to exceed the measured impedance range; only the high-frequency foot is visible, projected toward the imaginary axis. This is consistent with a parallel RC element of very large resistance and small capacitance, where the characteristic relaxation frequency falls below the lower measurement limit. As RH increases, resistance decreases progressively, the full semicircle becomes resolvable within the measurement window, and the arc diameter contracts systematically, reflecting enhanced charge transport through the sensing layer. This, in turn, confirms that the sensor is insensitive to humidity changes in this low range. Fig. 12b presents a qualitative overview of the impedance evolution across all measured RH levels. Quantitative equivalent circuit analysis and fitted spectra are presented separately in Fig. 13 for the humidity levels where the full semicircular arc was captured within the reliable measurement window. The humidity sensing mechanism of oxides is governed by the interaction between the surface of the oxides and adsorbed water molecules and the corresponding modulation in electrical properties.

For this low humidity range, the water molecules are adsorbed on the surface of the oxide through coordination with surface metal cations (Mg^{2+}, Fe^{3+}) and oxygen anions. The adsorbed water molecules dissociate and react with surface lattice oxygen (O^{2-}) to form hydroxyl groups as described by the following equation:

$$H_2O + O^{2-}\ 2OH^-$$

At this stage, the surface of the sensor is covered with a layer of chemically bonded hydroxyl groups; hence, the charges are localized. This corresponds to a high impedance value and phase angle near −90°, referring to capacitive-dominated behavior. Further increasing in humidity level resulted in physisorption of additional water molecules onto the pre-existing hydroxyl layer *via* hydrogen bonding. The physisorbed water molecules are mobile, where the proton can jump from surface hydroxyl groups to adjacent water molecules, initiating the Grotthuss mechanism. This stage can be described by the following equation:

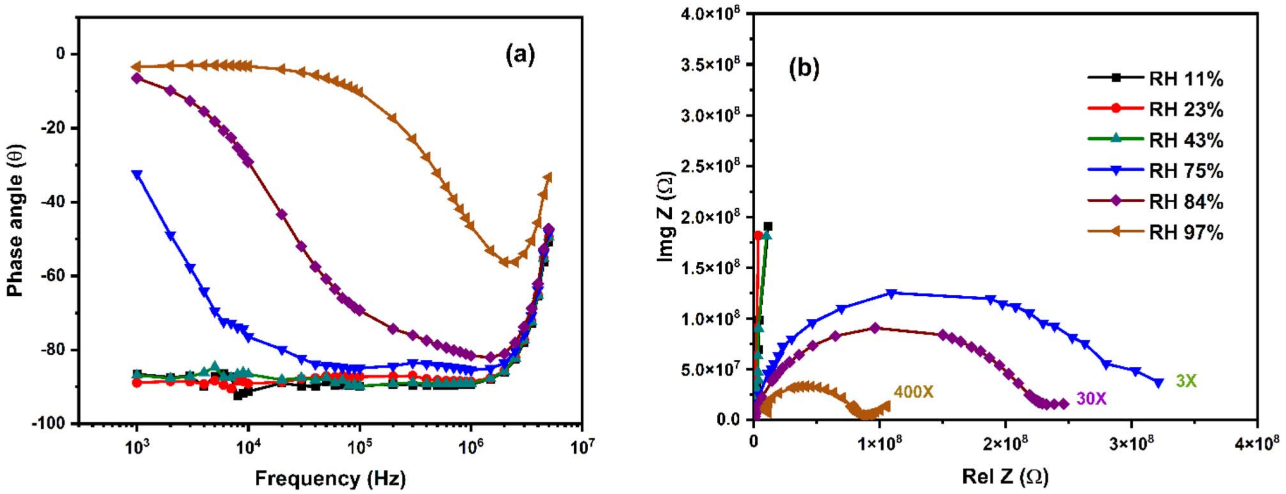

Fig. 12 (a) Phase angle and (b) Nyquist plot of the fabricated sensor at different RH levels as indicated, showing the qualitative evolution of the impedance response across the full humidity range.

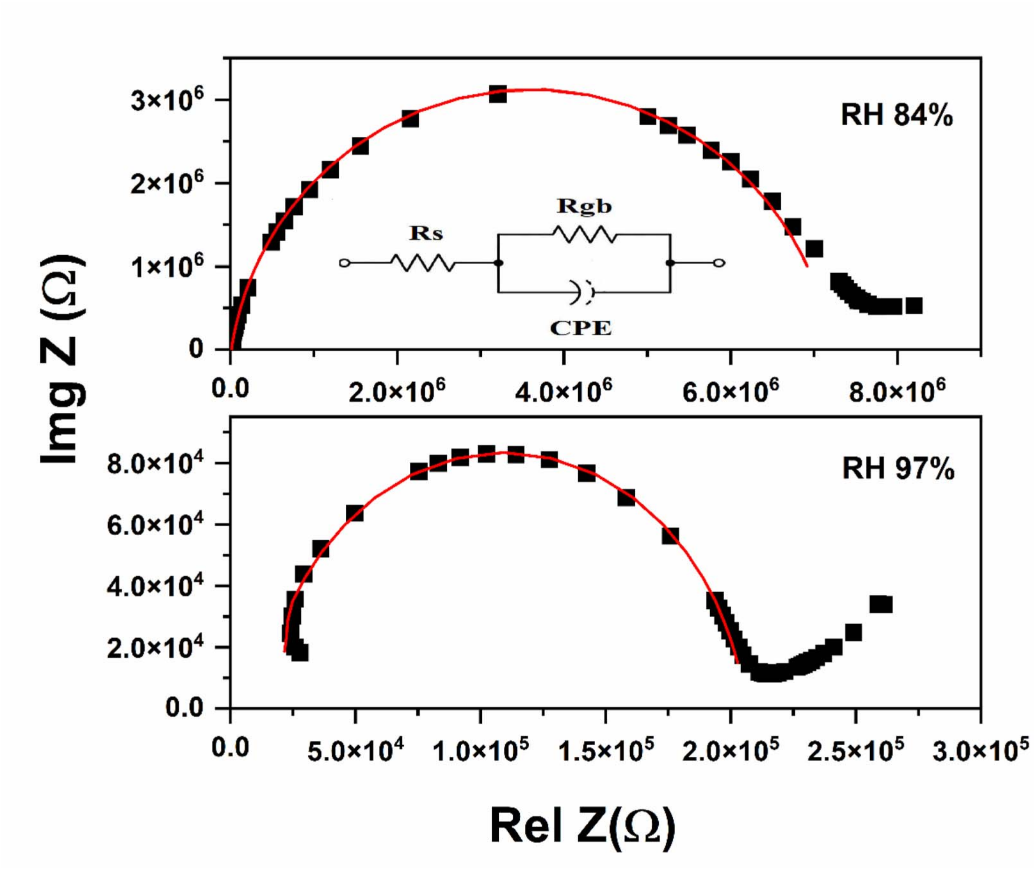

Fig. 13 Quantitative Nyquist plots at RH 84%, and 97% with experimental data (symbols) and fitted curves (solid lines) obtained from the R_s + (R_{gb}||CPE_{gb}) equivalent circuit model. These are the only humidity levels where the full semicircular arc was captured within the reliable measurement window. The equivalent circuit diagram is shown as an inset. Each panel uses an individual axis scale to resolve the semicircular arc at each RH level.

$$OH^- + H_2O \rightarrow O^{2-} + H_3O^+$$

$$H_3O^+ + H_2O \rightarrow H_2O + H_3O^+$$

When relative humidity exceeds 75%, multiple water layers are physisorbed, forming a continuous water film, where the water molecules behaves like bulk liquid water, thereby the Grotthuss mechanism becomes dominant.

$$H_3O^+ + H_2O \rightarrow H_3O^+ + H_2O$$

Based on the above discussion, the conduction mechanism is protonic *via* the Grotthuss mechanism. This mechanism reflected on the behavior of the sensor, where a transition from capacitive at low humidity levels with high impedance and high angle (−90°) resistive behavior at high humidity levels with low impedance and phase angle reaches zero.[4]

The Nyquist plot also experiences a change in its shape as the humidity increases. The shape of the Nyquist curves becomes semicircles. At very high humidity levels, the Nyquist showed a depressed semicircle with a tail. The diameter of the semicircle is related to the impedance value. As humidity increases, the semicircle diameter shrinks significantly, indicating the free movement of charge carriers due to water film formation. At 97% RH, the Nyquist plot shows a depressed semicircle with a tail-like feature at low frequencies. The measurement window (1 kHz – 5 MHz) does not extend to sufficiently low frequencies to allow reliable quantitative analysis of this region.

In principle, the impedance response of a polycrystalline material contains separate contributions from grain interior and grain boundary relaxations, appearing as two distinct arcs in the Nyquist representation. However, their resolution requires that both characteristic relaxation frequencies fall within the measurement window simultaneously. In the present data, the grain boundary resistance dominates the response at RH 75–97%, with its characteristic frequency falling at the lower edge of the measurement window. The grain interior arc, expected at significantly higher frequencies, is not resolved within the available measurement range. Consequently, the two contributions are spectrally inseparable under the present measurement conditions, and the equivalent circuit model $Z = R_s + (R_{gb}||CPE_{gb})$ was applied, where R_s subsumes the unresolved grain interior resistance. This limitation is inherent to the high resistivity of the material at these humidity levels and is consistent with the observation that the full grain boundary arc only becomes resolvable above 75% RH, where the resistance has decreased sufficiently to shift the relaxation frequency into the accessible window.

To quantitatively analyze the impedance response, the equivalent circuit model $R_s + (R_{gb}\|CPE_{gb})$ was applied, as shown in Fig. 13. Here, R_s is the series resistance representing the combined bulk grain and contact resistance. R_{gb} is the grain boundary resistance. CPE_{gb} is a constant phase element describing the non-ideal capacitive behavior at grain boundaries. The impedance of the CPE is defined as $Z_{CPE} = 1/[Q(j\omega)^n]$, where Q is the CPE constant in units of $S \times s^n$, n is the depression parameter ranging from 0 to 1, and ω is the angular frequency.[43] The effective capacitance that best represents the grain boundary response can be obtained from $C_{eff} = \sqrt[n]{Q R_{gb}^{(1-n)}}$.

At RH 11%, 23%, and 43%, the phase angle approaches $-90°$ across the entire measurement window from 1 kHz to 5 MHz, and the response appears linear, which both indicate a purely capacitive response with no resolvable semicircle. Resistance parameters cannot be extracted for these conditions. At RH 84%, and 97%, a depressed semicircle is progressively resolved within the measurement window. The separate Nyquist plots with fitted curves (at RH 84%, and 97%) and the equivalent circuit diagram are shown in Fig. 13. Fitting was performed for these two conditions, and the extracted parameters are reported in Table 5.

R_s was obtained from the fits but cannot be independently separated into its grain and contact contributions, as the grain arc is not resolved within the measurement window. The analysis therefore focuses on the grain boundary parameters R_{gb}, Q, n, and f_{peak}. The grain boundary resistance R_{gb} decreases from $7.29 \times 10^6\ \Omega$ at 84% RH to $1.94 \times 10^5\ \Omega$ at 97% RH, confirming that water adsorption progressively reduces grain boundary resistance and enhances charge transport. This progressive reduction in R_{gb} is consistent with adsorbed water film formation at grain boundary sites, which generates mobile protons and supports protonic conduction *via* the Grotthuss mechanism with increasing RH. The effective grain boundary capacitance C_{eff} decreases from 1.85×10^{-11} F at 84% RH to 1.33×10^{-12} F at 97% RH. This decrease is consistent with the progressive transition of the grain boundary response from capacitive-dominated to conduction-dominated behavior as RH increases. As R_{gb} drops by more than two orders of magnitude across this range, protonic conduction through the grain boundary becomes dominant, reducing the effective capacitive contribution of the interface. This interpretation is consistent with the phase angle shifting away from $-90°$ toward 0° at low frequencies with increasing RH, confirming that the grain boundary transitions from a capacitive to a resistive interface as water film formation advances. The apparent variation in Q across RH levels reflects the dependence of Q units on n and is not a physical discontinuity. The depression parameter n ranges from 0.91 to 0.905, indicating behavior close to an ideal capacitor and consistent with moderate grain boundary heterogeneity. The phase angle plot (Fig. 12a) independently supports the impedance analysis. The frequency of minimum phase angle shifts progressively from the low-frequency edge at 75% RH toward higher frequencies at 97% RH, consistent with the progressive reduction in R_{gb}. The overlapping phase angle curves at 11%, 23%, and 43% RH confirm purely capacitive behavior across the entire measurement window in this range.

All impedance measurements were performed over the frequency range of 1 kHz to 5 MHz. Data points near the lower frequency edge of 1 kHz showed behavior inconsistent with the dominant grain boundary relaxation arc described by the $R_s + (R_{gb}\|CPE_{gb})$ model. These points were excluded from the fitting, as their inclusion would require additional circuit elements that cannot be reliably parameterized within the available frequency window.

3.8 Dielectric and conductivity analysis

The dielectric features described below are discussed in direct relation to the humidity sensing mechanism and the RH-dependent sensor response. Fig. 14 shows the dielectric response at different RH levels. The frequency dependence of the complex permittivity is presented through the real part ε' (Fig. 14a) and the imaginary part ε'' (Fig. 14b). The corresponding AC conductivity is shown in Fig. 14c for different frequencies and RH conditions. The real permittivity (ε') decreases with increasing frequency in all RH levels.[34] A low-frequency dispersion appears, followed by flattening at higher frequencies. Above 1 MHz, there is another fall, or another dispersion starts to evolve. The dispersion becomes stronger and spans to higher frequencies with increasing RH. The flat frequency-independent part shifts up to higher values in the *y*-axis while shrinking in the *x*-axis.

The imaginary permittivity (ε'') decreases with frequency at low and mid ranges but shows a loss peak and then a partial increase at the highest frequencies. The noticed relaxation peak shifts progressively toward higher frequency with increasing RH. Above 1 MHz, ε' decreases further while ε'' exhibits a renewed rise whose peak lies beyond the upper measurement limit. This high-frequency feature shifts systematically with RH, indicating it is not a fixed structural relaxation but is driven by the humidity-dependent increase in mobile carrier density. In the low-frequency region (<10 kHz), ε' shows very high values,

Table 5 Equivalent circuit parameters from $R_s + (R_{gb}\|CPE_{gb})$ fitting at RH 84%, and 97%. Q and n: CPE parameters. C_{eff}: effective capacitance. f_{peak}: characteristic relaxation frequency

RH (%)	R_s (kΩ)	R_{gb} (Ω)	Q_{gb} ($S \times s^n$)	n_{gb}	C_{eff} (F)	f_{peak} (Hz)
84	19.3	7.29×10^6	4.119×10^{-11}	0.91	1.85×10^{-11}	1.18×10^3
97	10.9	1.94×10^5	5.603×10^{-12}	0.905	1.33×10^{-12}	618.91×10^3

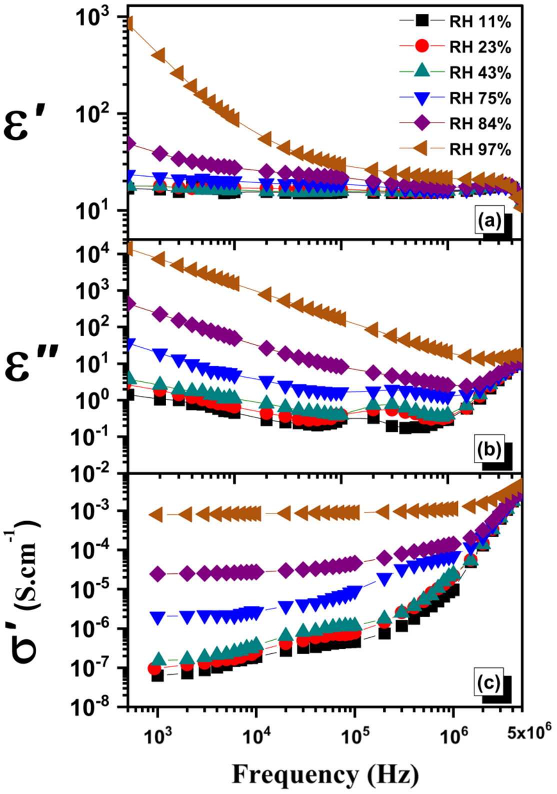

Fig. 14 The dielectric permittivity, ε', (a), the dielectric loss, ε'', (b), and AC conductivity, σ', (c) *vs.* frequency at different RH as indicated.

especially at higher RH levels, while ε'' also shows high values that gradually decay with frequency. In this region, both permittivity components (ε' and ε'') increase notably with RH. Curves show large slopes at higher RH, and the dispersion is stronger and extends over a wider frequency range with increasing RH. In the frequency range (10 kHz – 1 MHz), ε' decreases with frequency but not as rapidly as in the low-frequency region, and it exhibits relaxation-type dispersion. The RH dependence is most obvious at low frequencies, where interfacial and electrode-related polarizations are strongly RH sensitive and dominate the low-frequency response. The peak height of ε'' decreases systematically as RH increases, and the peak becomes progressively suppressed by the rising conductivity background. This relaxation peak is attributed to proton-hopping dynamics and dipolar reorientation of adsorbed water molecules, consistent with the Grotthuss-type protonic transport identified throughout this work. Notably, this peak persists across RH 11–84%, shifting progressively but remaining within the 10 kHz – 1 MHz window across this range and clearing the upper measurement limit only at RH 97%. The relaxation time τ was estimated from the fitted loss peak frequency as $\tau = 1/(2\pi f_{\text{peak}})$. τ decreases from 1.13×10^{-6} s at RH 11% to 5.35×10^{-7} s at RH 23%, 5.29×10^{-7} s at RH 43%, and to 4.39×10^{-7} s at RH 75%, confirming progressive acceleration of proton-hopping dynamics with humidity. At low and moderate RH levels, however, the extracted relaxation times carry significant uncertainty because the strong conductive background partially overlaps with the loss peak, making precise peak frequency determination less reliable than at higher RH levels. The significant shortening occurs between RH 11% and 23%, consistent with first-monolayer water adsorption establishing the primary proton-transfer pathway, after which τ stabilizes near 4–5 $\times$ 10^{-7} s while long-range conductivity continues to rise. Temperature-dependent measurements were outside the scope of this study; the RH dependence of τ serves as the primary quantitative descriptor of charge dynamics. The permittivity displays an inflection or a change in slope in the same frequency zone where the loss peak occurs. At frequencies above 1 MHz, ε' continues to decrease with increasing frequency, showing high-frequency dielectric dispersion while ε'' exhibits a renewed rise at the highest frequencies after the loss peak. The renewed ε'' increment coincides with the ε' drop. The magnitude of ε'' upturn grows with RH increase. At high RH levels and above 1 MHz, ε' and ε'' curves become smoother and closer. The increased RH level increases both permittivity and loss at all frequencies. The RH dependence for both ε' and ε'' is more obvious at low frequencies and higher RH levels. Both permittivity and loss values at 97% RH exceed low-RH values by orders of magnitude at low frequency.

The decrease in ε' with increasing frequency in all RH levels represents dispersion from polarization mechanisms unable to follow faster fields. The permittivity is dominated by slow polarizations at low frequency, as contributions fall off with increased frequency ($\omega = 1/\tau$). The flattening that follows the low-frequency dispersion region is caused by the limited time for relaxation processes to follow the field as frequency increases. The permittivity starts as a combination of slow interfacial, space-charge, and dipolar polarizations and produces large ε' at low frequencies; as frequency increases, these slow contributions fade and ε' approaches its background level, where the response time to field variations is limited. Above 1 MHz, we see another permittivity drop or a new dispersion evolving, which indicates the presence of a faster relaxation or likely conduction-related dispersion. The low-frequency dispersion strength increases and spans to higher frequencies with RH; this is caused by increased water content and mobile charges, which reduce relaxation times and/or add faster mobile carriers, shifting dispersive features upward. The flat, frequency-independent plateau shifts up in ε' (y-axis) because the low-frequency polarization magnitude grows with RH, while shrinking in frequency span (x-axis) because faster processes take over. The dielectric loss behavior results from a combination of relaxation dynamics. The low-frequency region is overwhelmed with conductivity contributions that appear as a linear drop, masking any other present relaxation. The loss peaks are contributions from conductivity and overlapping fast relaxation. The relaxation peak shifts progressively with increasing RH because higher humidity alters the local environment, reduces the relaxation time (τ), and moves the peak frequency (f_{peak}) toward higher values.[37] Above 1 MHz, ε' decreases further while ε'' rises again, forming a new peak out of range and shifting with RH, which is caused by either an unresolved fast relaxation appearing beyond the measured band or a rising $\sigma(\omega)/(\varepsilon_0\omega)$ term from increasing AC conductivity; both shift with RH.

In the low-frequency region (<10 kHz), ε' is very high, especially at high RH due to strong interfacial/Maxwell–Wagner-type polarization and surface water layers increasing effective capacitance; also, ε'' has high values and drops with frequency. This large loss results from slow charge accumulation that diminishes as frequency rises. Both ε' and ε'' increase notably with RH in the low-frequency region because higher RH means more adsorbed water, more dipoles and mobile ions, and larger storage and dissipation. The curves show large slopes at high RH, and the dispersion extends over a wider frequency range. This is caused by the broadened distribution of relaxation times and additional conduction channels activated by humidity. In the frequency range 10 kHz – 1 MHz, ε' decreases more slowly than at low frequency because in this span, remaining mid-speed dipolar or interfacial processes still contribute to this band. The loss relaxation peak shifts to a higher frequency with RH because RH accelerates dipole reorientation or proton hopping. The peak height decreases systematically with RH for two reasons. First, the growing conductivity background raises the ε'' baseline, reducing the peak-to-background contrast and suppressing the apparent relaxation strength. Second, increasing hydration broadens the distribution of relaxation times, spreading the response over a wider frequency range and producing an intrinsically shallower, more diffuse peak independent of the conductivity contribution. The magnitude of ε'' upturn grows with RH because RH increases the mobile carrier density and ionic/protonic conduction, enhancing the high-frequency loss contribution. The increased RH raises both permittivity and the loss at all frequencies because it adds more polar species and carriers that increase storage and dissipation. The RH dependence is most obvious at low frequencies, where interfacial and electrode-related polarizations are strongly RH sensitive and dominate the low-frequency response. Both permittivity and loss at 97% RH exceed low-RH values by orders of magnitude at low frequency because at this RH level, there are near-continuous adsorbed water films, and high carrier concentration produces very large ε' and ε'' at low frequency.

From our previous discussions regarding phase angle and impedance, we noticed that the phase angle is near −90° at low RH and low frequency, then moves toward 0° at high frequency and high RH, matching the transition from capacitive to resistive behavior seen in ε' and ε''.[5] The decrease in impedance with RH corresponds to the rise in both ε' and ε'', confirming increased charge transport and polarization. The loss peak in ε'' aligns with the phase angle drop, indicating the onset of conductive relaxation. Above 1 MHz, smoother ε' and ε'' curves agree with reduced impedance semicircle diameter, showing enhanced ion mobility. High RH causes both permittivity and conductivity features to evolve consistently with Nyquist compression and phase angle flattening. Above 1 MHz, no clear peak forms; ε'' only shows an upturn while ε' keeps decreasing, showing a dispersion tail. This behavior comes from fast polarization and conduction overlap, not new relaxation. The frequency is too high for interfacial or dipolar polarizations to respond, so the response is conduction-dominated at these frequencies. This aligns with phase angle dropping toward 0° and Nyquist semicircles shrinking with extended tails, both indicating resistive, conduction-dominated behavior at high RH and high frequency.

AC conductivity increases with frequency and with RH.[37] The response shows two main regimes: low-frequency behavior dominated by interfacial/electrode effects and surface-water-film conduction, and mid-to high-frequency dispersive behavior dominated by localized hopping and protonic transport. At RH ≤ 84%, the proton-hopping relaxation peak identified in the ε'' spectra falls within this dispersive window, precluding reliable extraction of the Jonscher exponent n. At RH 97%, where this peak has cleared the upper measurement limit, the AC conductivity follows Jonscher's power law with $n = 0.71$, confirming correlated ionic/protonic hopping as the dominant conduction mechanism. At higher humidity levels, the conductivity rises by several orders of magnitude. Two frequency regimes can be identified. At low frequencies, a near-plateau region is present. At mid and high frequencies, conduction is controlled by localized hopping and proton motion, and the frequency dependence indicates AC dispersive transport. At RH ≥ 75% this plateau is well-defined and σ_{dc} is read directly from it; at RH ≤ 43%, electrode polarization and the proton-hopping relaxation contribution obscure a clean plateau, and σ_{dc} is estimated from the low-frequency conductivity minimum as a lower-bound approximation. The extracted σ_{dc} values increase from 6.35×10^{-8} S m^{-1} at RH 11% to 9.53×10^{-8} S m^{-1} at RH 23%, 1.52×10^{-7} S m^{-1} at RH 43%, 2.1×10^{-6} S m^{-1} at RH 75%, 2.4×10^{-5} S m^{-1} at RH 84%, and 7.9×10^{-4} S m^{-1} at RH 97%, spanning nearly four orders of magnitude across the measured RH range. At higher frequencies, $\sigma(\omega)$ becomes dispersive and follows a power-law rise. At low frequency, conduction is dominated by interfacial effects and surface water layers. Charge accumulates at grain boundaries and electrode interfaces. This produces high conductivity at high humidity and low frequency. This behavior is not true bulk conduction. At mid and high frequencies, conduction is controlled by localized hopping and proton motion, and the frequency dependence indicates AC dispersive transport. The plateau amplitude and width grow with RH. The increased adsorbed water adds more charge carriers of mobile ions and protons (H^+/H_3O^+); this raises the DC-like conductivity, and hence the plateau amplitude increases. Higher carrier density reduces frequency dependence, keeps flat conduction behavior, and makes a longer or wider plateau. At higher RH, continuous water films form and connect surface sites. Connected paths allow long-range ionic flow. This increases the plateau level and makes it extend to higher frequencies. Increased humidity also makes charge motion faster. Water lowers the energy barrier for proton hopping. The relaxation time becomes shorter. Because of this, the transition from DC-like to frequency-dependent conduction moves to a higher frequency, so the plateau widens.

The conductivity trends directly follow the dielectric response [$\sigma(\omega) = \varepsilon_0 \times \omega \times \varepsilon''$]. Any increase or peak in ε''

produces a matching increase in $\sigma(\omega)$. The very high ε' values at low frequency and high humidity indicate strong interfacial polarization. This lowers impedance and increases conductivity. The shift of the ε'' relaxation peak to a higher frequency shows faster charge motion and higher conductivity. Across the full measured RH range (11–97%), permittivity, dielectric loss, and AC conductivity evolve consistently from a capacitive, polarization-dominated state at low humidity to a resistive, conduction-dominated state at high humidity. At low RH, slow interfacial polarizations produce large permittivity values but negligible long-range conduction, corresponding to the high-impedance, capacitive sensor state. As RH increases, adsorbed water populates surface hydroxyl sites, generating mobile protons and hydronium ions that reduce relaxation times, shift the loss peak to higher frequencies, and raise the DC-like conductivity plateau by several orders of magnitude. The increased polar species and mobile carrier density collectively raise both permittivity and dielectric loss across the entire measured frequency range. The most pronounced changes occur between 43% and 97% RH, where connected water films form and long-range protonic transport *via* the Grotthuss mechanism becomes dominant. The widening conductivity plateau, upward permittivity dispersion shift, and loss peak migration are markers of this progressive surface hydration. The impedance decrease and capacitance increase defining the sensor output are the macroscopic electrical consequences of these microscopic changes, confirming that the dielectric response and sensing response are two perspectives on the same physical process, where surface-water-film-controlled protonic conduction operates as the dominant humidity transduction mechanism in Mg_2FeVO_6.

4 Conclusion

This work provides the first study focusing on the humidity-dependent electrical and dielectric properties of Mg_2FeVO_6. The Mg_2FeVO_6 was successfully synthesized by the sol–gel method. XRD identified three crystalline phases with high crystallinity and a dominant $Ia\text{-}\bar{3}d$ double perovskite-related structure with a crystallite size of 26.1 nm. The negative zeta potential and presence of surface hydroxyl groups support water adsorption on the material surface. A drop-cast humidity sensor fabricated on an FTO substrate showed a clear impedance and capacitance response to RH, with capacitance being about 48 times more sensitive than impedance. The response was non-linear, with a sharp change above 43% RH linked to continuous water film formation on the sensing surface. The sensor demonstrated good repeatability over four cycles and excellent short-term stability across all tested RH levels. The long response time of 760 s is a limitation attributed to diffusion-limited mass transport through the densely packed microstructure observed by SEM. The surface hydroxyl groups confirmed by zeta potential measurements indicate adequate surface reactivity. The fast recovery time of 25 s reflects the asymmetry between inward diffusion and surface desorption kinetics. Phase angle and complex impedance spectroscopy confirmed that the sensor transitions from capacitive-dominant behavior at low RH to resistive-dominant behavior at high RH. Dielectric spectroscopy showed that both real and imaginary permittivity and AC conductivity increase with RH at all frequencies. The relaxation peak shifts to a higher frequency with increasing RH, indicating shorter relaxation time and faster charge transport. Conduction is controlled by surface water films and grain boundaries, with protonic hopping as the dominant mechanism when water films form. This study provides the first humidity-dependent electrical and dielectric dataset for Mg_2FeVO_6 and establishes a baseline for evaluating double perovskite-related structure oxides in humidity sensing applications. Although the Mg_2FeVO_6 humidity sensor revealed excellent stability and sensitivity, however, the long response time is a limitation. Future strategies to address this include surface area maximization, porosity engineering, surface functionalization, and composite formation.

Ethical approval

Not applicable. This study does not contain any studies with human participants or animals performed by any of the authors.

Author contributions

Mohamed I. Farouk: data curation, funding acquisition, formal analysis, writing – original draft, writing – review & editing. A.G. Darwish: conceptualization, visualization, data curation, methodology, formal analysis, software, writing – original draft, writing – review & editing. Mohamed Morsy: methodology, conceptualization, data curation, formal analysis, writing – original draft, writing – review & editing.

Conflicts of interest

There are no conflicts of interest to declare.

Data availability

All the data supporting the findings of this study are included in this published article.

Supplementary information (SI): Table S1 complete XRD peak indexing for all 25 observed reflections. Fig. S1 observed XRD pattern of the magnesium iron vanadate ceramic. Inset: pseudo-Voigt profile fitting of the isolated (400) fundamental reflection of Phase A at $2\theta = 35.622°$. Table S2 complete peak assignment from Le Bail profile fitting. See DOI: https://doi.org/10.1039/d6ra02584f.

Acknowledgements

This work was supported and funded by the Deanship of Scientific Research at Imam Mohammad Ibn Saud Islamic University (IMSIU) (grant number IMSIU-DDRSP2602).

References

1 B. Arman Kuzubasoglu, Recent Studies on the Humidity Sensor: A Mini Review, *ACS Appl. Electron. Mater.*, 2022, **4**, 4797–4807, DOI: 10.1021/acsaelm.2c00721.

2 J.-M. Tulliani, B. Inserra and D. Ziegler, Carbon-Based Materials for Humidity Sensing: A Short Review, *Micromachines*, 2019, **10**, 232, DOI: 10.3390/mi10040232.

3 A. Kumar, G. Gupta, K. Bapna and D. D. Shivagan, Semiconductor-metal-oxide-based nano-composites for humidity sensing applications, *Mater. Res. Bull.*, 2023, **158**, 112053, DOI: 10.1016/j.materresbull.2022.112053.

4 J. Qian, R. Tan, M. Feng, W. Shen, D. Lv and W. Song, Humidity Sensing Using Polymers: A Critical Review of Current Technologies and Emerging Trends, *Chemosensors*, 2024, **12**, 230, DOI: 10.3390/chemosensors12110230.

5 T. Xie, A. F. Abdul Rahman, A. Abu Bakar and A. Arsad, Design and Optimization of Metal Oxide-Based Humidity Sensors: A Review on Mechanisms and Material Engineering, *J. Clust. Sci.*, 2025, **36**, 148, DOI: 10.1007/s10876-025-02869-0.

6 D. Han, Y. Wang, J. Li, M. Gao, Y. Luan, M. Shao and N. Ma, Perovskite-Based Humidity Sensor, *ACS Appl. Mater. Interfaces*, 2026, **18**, 3360–3377, DOI: 10.1021/acsami.5c17730.

7 A. A. Bhran, R. M. Sabry, M. A. Farag, A. G. Gadallah and A. G. Darwish, Multifunctional evaluation of dielectric, optical, magnetic, and methylene blue adsorption behaviors of Ba2FeVO6 double perovskite, *J. Mater. Sci. Mater. Electron.*, 2025, **36**, 2056, DOI: 10.1007/s10854-025-16088-w.

8 Y. Li, Y. Ding, J. Sun, S. Tan, Y. Li, X. Wang, J. Cai, J. Bai, X. Lv, W. Guo, Y. Hao, Y. Liu, Z. Lin and J. Chang, Design Strategies and Emerging Applications of Perovskite-Based Sensors, *SmartMat*, 2025, **6**(3), e70022, DOI: 10.1002/smm2.70022.

9 J. Sahu, B. N. Parida, N. C. Nayak, R. Padhee and S. K. Parida, Studies of structure, microstructure, dielectric, and electrical properties of Mg2FeVO6 ceramic for device application, *J. Electroceramics*, 2025, DOI: 10.1007/s10832-025-00439-4.

10 P. S. Padhi, S. K. Rai, H. Srivastava, R. S. Ajimsha, A. K. Srivastava and P. Misra, Maxwell–Wagner Relaxation-Driven High Dielectric Constant in Al 2 O 3/TiO 2 Nanolaminates Grown by Pulsed Laser Deposition, *ACS Appl. Mater. Interfaces*, 2022, **14**, 12873–12882, DOI: 10.1021/acsami.1c25028.

11 S. H. Khoreem and A. H. AL-Hammadi, Tailoring the functional properties of $BaNi_{2-x}Zn_xFe_{16}O_{27}$ ferrites *via* ceramic route for advanced electronic and energy applications, *Discov. Mater.*, 2025, **5**, 173, DOI: 10.1007/s43939-025-00374-9.

12 T. Kobayashi, T. Ikeda and A. Nakayama, Long-range proton and hydroxide ion transfer dynamics at the water/CeO 2 interface in the nanosecond regime: reactive molecular dynamics simulations and kinetic analysis, *Chem. Sci.*, 2024, **15**, 6816–6832, DOI: 10.1039/D4SC01422G.

13 C.-A. Ku and C.-K. Chung, Advances in Humidity Nanosensors and Their Application: Review, *Sensors*, 2023, **23**, 2328, DOI: 10.3390/s23042328.

14 W. Yu, D. Chen, J. Li and Z. Zhang, TiO2-SnS2 Nanoheterostructures for High-Performance Humidity Sensor, *Crystals*, 2023, **13**, 482, DOI: 10.3390/cryst13030482.

15 M. Morsy, A. I. Abdel-Salam, M. Mostafa and A. Elzwawy, Promoting the humidity sensing capabilities of titania nanorods/rGO nanocomposite *via* de-bundling and maximizing porosity and surface area through lyophilization, *Micro Nano Eng.*, 2022, **17**, 100163, DOI: 10.1016/j.mne.2022.100163.

16 A. I. Madbouly, M. Morsy and R. F. Alnahdi, Microwave-assisted synthesis of Co-doped SnO2/rGO for indoor humidity monitoring, *Ceram. Int.*, 2022, **48**, 13604–13614, DOI: 10.1016/j.ceramint.2022.01.240.

17 A. Altomare, M. C. Burla, C. Giacovazzo, A. Guagliardi, A. G. G. Moliterni, G. Polidori and R. Rizzi, Quanto : a Rietveld program for quantitative phase analysis of polycrystalline mixtures, *J. Appl. Crystallogr.*, 2001, **34**, 392–397, DOI: 10.1107/S0021889801002904.

18 S. P. A. Paz, H. Kahn and R. S. Angélica, A proposal for bauxite quality control using the combined Rietveld – Le Bail – Internal Standard PXRD Method – Part 1: hkl model developed for kaolinite, *Miner. Eng.*, 2018, **118**, 52–61, DOI: 10.1016/j.mineng.2018.01.006.

19 Á. X. Moreno Erazo, *Obtención tecnológica de mullita a partir de arcillas y caolines refractarios argentinos, y alúmina calcinada o alúminas hidratadas*, PhD thesis, Universidad Nacional de La Plata, La Plata, Argentina, 2014, DOI: 10.35537/10915/36815.

20 Z. Pei, X. Zhou, K. Leng, W. Xia, Y. Wei and X. Zhu, Structural characterizations and dielectric, magnetic, and optical properties of Ba2FeVO6 double perovskite ceramics, *AIP Adv.*, 2020, **10**, 075320, DOI: 10.1063/5.0011677.

21 R. D. Shannon, Revised effective ionic radii and systematic studies of interatomic distances in halides and chalcogenides, *Acta Crystallogr., Sect. A*, 1976, **32**, 751–767, DOI: 10.1107/S0567739476001551.

22 P. M. Woodward, Octahedral Tilting in Perovskites. I. Geometrical Considerations, *Acta Crystallogr. Sect. B Struct. Sci.*, 1997, **53**, 32–43, DOI: 10.1107/S0108768196010713.

23 G. King and P. M. Woodward, Cation ordering in perovskites, *J. Mater. Chem.*, 2010, **20**, 5785, DOI: 10.1039/b926757c.

24 S. Vasala and M. Karppinen, A2B′B″O6 perovskites: A review, *Prog. Solid State Chem.*, 2015, **43**, 1–36, DOI: 10.1016/j.progsolidstchem.2014.08.001.

25 V. M. Goldschmidt, Die Gesetze der Krystallochemie, *Naturwissenschaften*, 1926, **14**, 477–485, DOI: 10.1007/BF01507527.

26 F. Zhou, X. Tao, H. Wang, S. Guo, L. Jiao, Y. Zhang, Y. Wang, X. Yu, L. Ding, F. Zhang, Y. Gao and F. Wang, Vanadium as a superior promoter in LaFeO3 perovskite for "low-temperature" H2S catalytic oxidation with high sulfur deposition tolerance, *Appl. Catal. A Gen.*, 2026, **713**, 120812, DOI: 10.1016/j.apcata.2026.120812.

27 A. S. Al-Wasidi, F. K. Algethami, F. A. Saad and E. A. Abdelrahman, Remarkable High Adsorption of Methylene Blue Dye from Aqueous Solutions Using Facilely Synthesized MgFe2O4 Nanoparticles, *J. Inorg. Organomet. Polym. Mater.*, 2023, **33**, 2035–2045, DOI: 10.1007/s10904-023-02652-6.

28 I. Wayan Sutapa, A. Wahid Wahab, P. Taba and N. La Nafie, Synthesis and Structural Profile Analysis of the MgO Nanoparticles Produced Through the Sol-Gel Method Followed by Annealing Process, *Orient. J. Chem.*, 2018, **34**, 1016–1025, DOI: 10.13005/ojc/340252.

29 Y. Slimani, M. K. Hamad, I. O. Olarinoye, Y. S. Alajerami, M. I. Sayyed, M. A. Almessiere and M. H. A. Mhareb, Determination of structural features of different Perovskite ceramics and investigation of ionizing radiation shielding properties, *J. Mater. Sci. Mater. Electron.*, 2021, **32**, 20867–20881, DOI: 10.1007/s10854-021-06603-0.

30 N. Thanamoon, N. Thongyong, K. Sreejivungsa, N. Chanlek, W. Jarernboon and P. Thongbai, Outstanding dielectric permittivity and humidity sensitivity in (Y/Sb) codoped TiO2 ceramics with rapid response/recovery time, *Sensor. Actuator. B Chem.*, 2024, **419**, 136372, DOI: 10.1016/j.snb.2024.136372.

31 K. A. Stoerzinger, W. T. Hong, G. Azimi, L. Giordano, Y.-L. Lee, E. J. Crumlin, M. D. Biegalski, H. Bluhm, K. K. Varanasi and Y. Shao-Horn, Reactivity of Perovskites with Water: Role of Hydroxylation in Wetting and Implications for Oxygen Electrocatalysis, *J. Phys. Chem. C*, 2015, **119**, 18504–18512, DOI: 10.1021/acs.jpcc.5b06621.

32 C. M. Maguire, M. Rösslein, P. Wick and A. Prina-Mello, Characterisation of particles in solution – a perspective on light scattering and comparative technologies, *Sci. Technol. Adv. Mater.*, 2018, **19**, 732–745, DOI: 10.1080/14686996.2018.1517587.

33 A. M. Mansour, M. Morsy, A. M. El Nahrawy and A. B. Abou Hammad, Humidity sensing using Zn$(1.6-x)$Na0.4Cu$_x$TiO4 spinel nanostructures, *Sci. Rep.*, 2024, **14**, 562, DOI: 10.1038/s41598-023-50888-6.

34 N. Thanamoon, N. Thongyong, K. Sreejivungsa, N. Chanlek and P. Thongbai, Enhanced humidity-sensing performance of (Zr 4+/Sb 5+)-codoped TiO 2 ceramics with giant dielectric properties, *J. Adv. Ceram.*, 2025, **14**, 9221005, DOI: 10.26599/JAC.2024.9221005.

35 K. Sreejivungsa, N. Thanamoon, N. Phromviyo, W. Jarernboon, M. Takesada and P. Thongbai, Advanced humidity sensing properties of CuO ceramics, *Sci. Rep.*, 2024, **14**, 9726, DOI: 10.1038/s41598-024-60421-y.

36 C. Yang and H. Zhang, Preparation and performance study of humidity sensor based on defect-controlled TiO2/CdS heterostructure, *Sensors Actuators B Chem.*, 2024, **404**, 135321, DOI: 10.1016/j.snb.2024.135321.

37 D. L. Sekulić and T. B. Ivetić, Characterization of an Impedance-Type Humidity Sensor Based on Porous SnO2/TiO2 Composite Ceramics Modified with Molybdenum and Zinc, *Sensors*, 2023, **23**, 8261, DOI: 10.3390/s23198261.

38 S. Karamat, W. Majeed, M. D. Albaqami, M. Sheikh, M. Talha, U. Batool, Z. Imran, S. Khan and M. Kashif, High-performance humidity sensors based on reduced graphene oxide sheets decorated with cobalt and iron doped ZnO nanorods, *Mater. Today Commun.*, 2024, **40**, 109742, DOI: 10.1016/j.mtcomm.2024.109742.

39 A. F. F. Alaih, D. Triyono, M. A. Dwiputra and F. A. A. Nugroho, Ultrafast and low-hysteresis humidity sensors based on mesoporous LaFe0.925Ti0.075O3 perovskite, *Sensor. Actuator. B Chem.*, 2024, **412**, 135810, DOI: 10.1016/J.SNB.2024.135810.

40 M. Pi, D. Wu, J. Wang, K. Chen, J. He, J. Yang, D. Zhang, S. Chen and X. Tang, Real-time and ultrasensitive humidity sensor based on lead-free Cs2SnCl6 perovskites, *Sensors Actuators B Chem.*, 2022, **354**, 131084, DOI: 10.1016/j.snb.2021.131084.

41 M. Geng, X. Pan, J. Zhao, X. Wang, R. Liu, Z. Xu, N. Ma, M. Gao, M. Shao and J. Li, Regulating crystal growth of Cs2SnCl6 perovskite for rapid response and durable humidity-triggered non-contact sensor, *Chem. Eng. J.*, 2024, **486**, 150222, DOI: 10.1016/j.cej.2024.150222.

42 M.-Y. Cho, I.-S. Kim, S. Kim, C. Park, N.-Y. Kim, S.-W. Kim, S. Kim and J.-M. Oh, Unique Noncontact Monitoring of Human Respiration and Sweat Evaporation Using a CsPb 2 Br 5 -Based Sensor, *ACS Appl. Mater. Interfaces*, 2021, **13**, 5602–5613, DOI: 10.1021/acsami.0c21097.

43 B. Hirschorn, M. E. Orazem, B. Tribollet, V. Vivier, I. Frateur and M. Musiani, Determination of effective capacitance and film thickness from constant-phase-element parameters, *Electrochim. Acta*, 2010, **55**, 6218–6227, DOI: 10.1016/j.electacta.2009.10.065.